Chapter 6
Underpotential Deposition and Related Phenomena at the Nanoscale: Theory and Applications

6.1 General Aspects

Macroscopic materials composed by transition metals such as Ag, Au, Cu, Pd, and Pt are ductile, malleable, besides displaying excellent electrical and heat conductivity and high optical reflectivity. These properties have allowed these materials to be widely used in several areas, such as electronics (electrical contacts and conductors) and the catalysis of chemical reactions. When the size of these materials decreases to the nanometric scale, these particles show unique properties, which cannot be observed in macroscopic-sized materials. The number of synthesis methods of these nanomaterials and their new and possible technological applications has increasingly grown during the last decade. This progress has inevitably led to the commercialization of several nanomaterials. For example, Ag nanoparticles (NPs) have been used as a type of antimicrobial reactive of broad spectrum in medicine, mass consumer products, antiseptic aerosols of domestic use, antimicrobial water filters coatings, etc. [1]. Apart from these commercial applications, nanomaterials are largely used in the field of research, e.g. plasmonics, medicine, reactivity, combustion cells, etc. [2, 3].

These last decades have witnessed important advances in the development, the characterization and the way to assemble and/or produce molecular-scale devices. Nanoscience and Nanotechnology are the branches of science in charge of these advances. Nanotechnology consists of production, manipulation, and integration of devices at the nanoscale while Nanoscience provides the basic theoretical support for these achievements [4, 5].

Many construction processes, artificial as well as natural, occur at the nanoscale; this has inspired many different researchers all over the world to deepen into the fundamental study of matter at this scale. The new properties possible to be reached manipulating the matter at these size orders are unprecedented and for this reason, different authors predict that this technology will lead to a third industrial revolution much deeper than its predecessors.

© Springer International Publishing Switzerland 2016

O.A. Oviedo et al., *Underpotential Deposition*, Monographs in Electrochemistry,
DOI 10.1007/978-3-319-24394-8_6

Several examples clearly show that the physical parameters of nanomaterials such as size, shape, surface coating, and surrounding environment strongly influence their properties and, therefore, their performance in the applications. Different shapes of metallic nanomaterials are synthesized in a routine way; these include spheres, spheroids, cubes, cuboctahedrons, octahedrons, tetrahedrons, decahedrons, icosahedrons, thin plates, ribs or wires, stars, etc. To this aim, a great number of techniques, protocols, and manufacturing routines can be summarized in two types of strategies:

(a) Top-Down, also known as conventional manufacturing: it starts from the big objects which are then broken down into smaller objects. This type of strategy has characterized the technological advances of the last century. Some common examples are the technologies used for the manufacture of microprocessors, hard disks based on giant magnetoresistance, focused ion beams, atomic force microscope tips used as a writing device, etc.
(b) Bottom-up, also known as molecular manufacturing: small individual elements are linked together in order to form bigger components with a superior hierarchy, which then in turn are linked to each other until an even bigger system is formed. For instance, the manufacturing processes that utilize the specificity of Watson-Crick base pairing to build DNA and other nucleic acids well-defined structures, the chemical and/or electrochemical synthesis (organic and inorganic synthesis) aim to design molecules with well-defined shape, molecular self-assembly for automatic ordering, etc. It is expected that this type of strategy will prevail in the present century.

Bottom-up methods allow smaller geometries than Top-Down ones and are generally more economical. Today we face a dramatic transition stage between these two strategies [1–6].

But, what makes nanothecnology or nanoscience scientifically interesting? This question has many answers, but perhaps the one of greater importance is that many of the nanosystems properties can be tuned by controlling the size, shape and composition of nanosystems. Such is the importance of this topic that a complete book has been devoted to it [7]. In general, nanomaterials properties separate from the macroscopic laws of Physics; however, these properties can be rationalized considering quantum mechanics and/or nanothermodynamics. Ligand molecules generally coordinate small metallic clusters, commonly less than 1 nm in diameter, and their behavior is similar to that of a single molecule. In contrast, properties of metallic NPs, greater than 1 nm in diameter, can be considered as intermediate cases between the properties of a single molecule and the properties of bulk material. The following example can help to a better understanding of this situation. The melting point of a solid is, in a classical way, a constant, an intensive property of the matter; it is even utilized in the laboratories initial lessons at chemistry university studies as a method of identification. This picture may not occur at the nanoscale. It is well-known that the melting point of a bulky piece of Au is approximately 1337 K, but Au-NPs of approximately 20 nm in diameter start melting at lower temperatures. The melting point dramatically falls in sizes ranging

from 3 to 4 nm [8], while for a Au nanocluster of 1.5 nm, it can fall down to 775 K [7].

What effect does nano-size have on the chemical properties of materials? The answer will be given through another example. The chemical potential of a component's system, μ, is defined as the differential change of Gibbs free energy, G, given the addition of a new particle to the system, N, maintaining all the other variables constant. Mathematically speaking this corresponds to:

$$\left(\frac{\partial G}{\partial N}\right)_{P,T} = \frac{G}{N} = \mu \tag{6.1}$$

If the system is infinite (bulk), both equalities in Eq. (6.1) are then fulfilled. In other words, the chemical potential is only a function of pressure (P) and temperature (T), that is, we can write $\mu(P,T)$. Let us consider now a NP of the same material, at the same P and T conditions. The NP chemical potential, called μ^{NP}, is:

$$\left(\frac{\partial G}{\partial N}\right)_{P,T} \approx \mu + \alpha N^{-1/3} \approx \mu^{\mathrm{NP}} \tag{6.2}$$

where α is a surface free energy per atom, $N^{-1/3}$ appears as a consequence that the number of surface atoms is proportional to N to the power 2/3. It is worth mentioning that Eq. (6.2) is a first approach to the chemical potential of a NP. If the NP was of a smaller size or free standing, other contributions should be added to Eq. (6.2), such as curvature and rotational terms. The mathematical expression for μ^{NP} depends on the model used to describe it. The most used version consists in assuming a spherically-shaped NP where $\alpha N^{-1/3} = (2M\gamma)/(zF\rho r)$ where M, γ, z, F, ρ and r correspond to the molar mass, surface energy, cation charge, Faraday constant, specific mass and NP radius, respectively. This is known in the literature as Gibbs-Thomson Model. As the NP gets smaller, the second term on the right hand side of Eq. (6.2) becomes relatively more important and subsequently, major deviations from the bulk behavior will appear. It is intuitive to infer from Eq. (6.2) that at the nanoscale, the chemical potential is not only a function of both: P and T, but also of the NP size as well, that is $\mu^{\mathrm{NP}}(P,T,N)$.

What effect does nano-size have on the electrochemical properties of materials? We will attempt an answer by analyzing the effect on the Fermi level of a metal (ε_{F}). The latter magnitude is defined as the electrochemical potential of the electrons inside a metal ($\widetilde{\mu}_{\mathrm{e}}$). The work function ($\Phi$), is the minimum work necessary to remove an electron from the Fermi level to the vacuum:

$$\Phi = -\varepsilon_{\mathrm{F}} - e_0\phi \tag{6.3}$$

where ϕ is the electrostatic potential right outside of the metal. The vacuum level is the energy of an electron at rest at a point far enough from the surface that the electrostatic image force can be despised – typically at 10 nm from the surface [9].

If the electrode is infinitely large, then Φ has a well-defined value for a given metal and surface structure. Conversely, for spherical metal NPs of intermediate sizes, the electron removal energy has been found to scale as [10]:

$$\Phi^{NP} = \Phi - \left[\frac{2M\gamma}{zF\rho} - \frac{5}{8}e_0^2\right]\frac{1}{r} \tag{6.4}$$

where Φ^{NP} corresponds to the NP work function. The term $2M\gamma/(zF\rho)$, appears from considering the change of the NP chemical potential according to the Gibbs-Thomson model [11], as presented in the discussion following Eq. (6.2). The term $5e_0^2/8$ corresponds to the corrections of the image-charge contributions according to a classical model introduced by Wood and Plieth [12, 13]. Thus, work function size dependence may be considered as the addition of two terms: first, the chemical potential change of the electrons in the metal particle and second, the image force change. If a NP is used as a nanoelectrode, the position of its Fermi level regarding the molecular orbitals of the redox species in solution may change; consequently, its electrochemical behavior may be different. In general for a metal, the dipolar contribution is greater than chemical contribution, so extracting an electron from a NP sometimes involves a larger work than taking it out from the corresponding bulk material and the smaller the NP is, the larger this work will become. Thus, this early work showed that "nano" effects might become important in electrochemical processes where the work function is known to play a key role, for example in determining the potential of zero charge of the electrode. For instance, Schnippering et al. [14] showed that the work function of Ag particles, Φ_{Ag}^{NP} increased from (5.29 ± 0.05) to (5.53 ± 0.05) eV as the particle size decreased ranging from 35 to 4 nm. These values are approximately 1.01 to 0.55 eV higher than for monocrystalline Ag surfaces (4.74, 4.64, and 4.52 eV for [111], [100], and [110] surface, respectively [8]). As it is mentioned by the authors, this great difference is also partly attributed to the surface dipole induced by the link citrate-Au (surface) (about 0.2 eV) and the presence of an oxide film on the Ag-NPs surface. However, disregarding these contributions, the tendency to increase Φ_{Ag}^{NP} with the size is still clear.

6.2 Kinetics and Thermodynamic Driving Force

6.2.1 Reduction Mechanism

The reduction of aqueous metallic oxidized species, $M_{(aq)}^{z+}$, leads to neutral atoms and these constitute the construction blocks of clusters and metallic NPs. This process is the result of consecutive redox reactions in which the electrons of a reducing agent, Red^{u}, are transferred to the metal according to the following electrochemical equations:

$$m\mathrm{M}^{z+}_{(\mathrm{aq})} + (mz)\mathrm{e}^- \rightarrow \mathrm{M}^0_{\mathrm{m}} \tag{6.5}$$

$$\mathrm{Red}^u \rightarrow \mathrm{Ox}^{u+1} + \mathrm{e}^- \tag{6.6}$$

$$m\mathrm{M}^{z+}_{(\mathrm{aq})} + (mz)\mathrm{Red}^u \rightarrow (mz)\mathrm{Ox}^{u+1} + \mathrm{M}^0_m \tag{6.7}$$

where Ox^{u+1} is the oxidized species. The driving force of the process is the difference between the redox potentials, ΔE, between reactions (6.5) and (6.6). The magnitude of ΔE determines the value of the equilibrium constant, K, of reaction (6.7) according to:

$$\ln K = \frac{zF}{RT}\Delta E \tag{6.8}$$

The reduction reaction of $\mathrm{M}^{z+}_{(\mathrm{aq})}$ is thermodynamically possible only if ΔE is positive, which implies that the redox potential of the reducing agent must have a more negative value than that of the metallic species. From a practical viewpoint, this difference must be greater than about 0.4 V, otherwise, it will not be able to start, or it will proceed at a very slow speed. For example, for the Au o Pt cases, two metals with high reduction potentials ($E^0_{\mathrm{Au}^+/\mathrm{Au}} = 1.692$ V and $E^0_{\mathrm{Pt}^{2+}/\mathrm{Pt}} = 1.18$ V), the reduction process may occur with weak reducing agents. On the contrary, metals with low reduction potentials such as Cr ($E^0_{\mathrm{Cr}^{2+}/\mathrm{Cr}} = -0.913$ V) require stronger reducing agents and more extreme reaction conditions.

If the metal ion intervening in reaction (6.5) is complexed in aqueous solution or if it is part of a compound, the standard redox potential, E^0 will be smaller. The decrease of redox potential depends on the stability of these complexes; for instance, Table 6.1 shows the changes occurring in the Ag ion standard potential due to the formation of complexes with an increase in the stability. These different stabilities limit the selection of the reducing agents.

Another alternative to modify E^0 is the use of the acid–base reactions, which are generally coupled to the reduction reactions. The reaction *p*H has a strong impact on the solute redox potentials and this impact can be quantified by Nernst equation. Both, complexing and *p*H effects, can be condensed in the so-called "redox diagrams". These provide detailed information about the way to manipulate the reaction conditions in order to generate metallic NPs with the desired structure and size. As an example, Fig. 6.1 shows the redox diagram of Pd^{2+}, Ag^+ and hydrazine when the pH of the solution is adjusted with ammonia, which strongly makes both cations complexed. The corresponding redox reactions are inserted in the Figure.

According to Eq. (6.8) an increase in the value of ΔE will translate into a more spontaneous reaction, leading to smaller sized metal particles due to the generation of a larger number of nuclei. The size of the metal particles decreases as ΔE of the reaction increases. So, reduction reactions with very large ΔE must be employed to generate nanosized metal particles, which implies the selection of uncomplexed

Table 6.1 Changes on the Ag^+ redox potential as the result of the formation of different complexes in aqueous solution

Redox system	E^0/V
$Ag^+ + e^- \rightarrow Ag^0$	0.799
$[Ag(NH_3)_2]^+ + e^- \rightarrow Ag^0$	0.38
$[Ag(SO_3)_2]^{3-} + e^- \rightarrow Ag^0 + 2SO_3^{2-}$	0.29
$[Ag(S_2O_3)_2]^{3-} + e^- \rightarrow Ag^0 + 2S_2O_3^{2-}$	0.01
$[AgI_4]^{3-} + e^- \rightarrow Ag^0 + 4I^-$	−0.09
$[Ag(CN)_3]^{2-} + e^- \rightarrow Ag^0 + 3CN^-$	−0.51

Reedited with permission from Ref. [15]

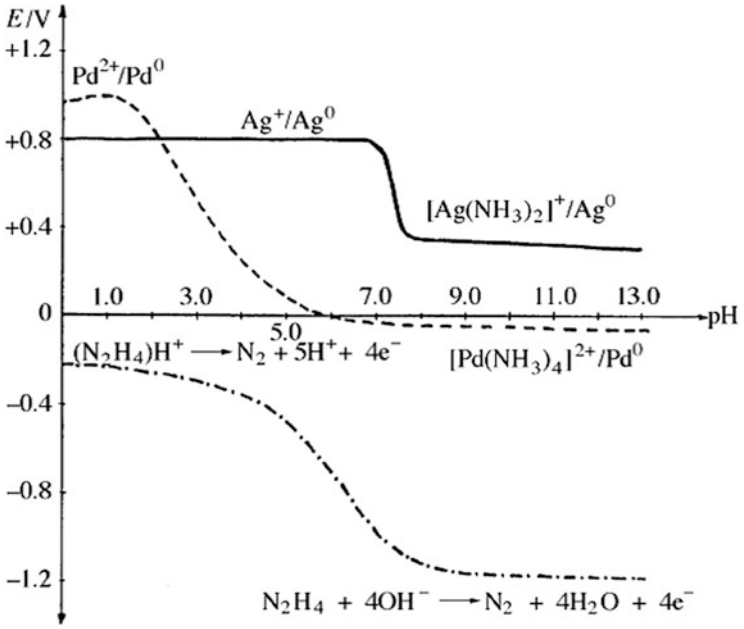

Fig. 6.1 pH effect on the hydrazine redox potential and the complex ammonium-Metallic of palladium and silver (Reprinted with permission from Ref. [56])

metal ions coupled with very strong reducing agents. The requirement of a large ΔE is a necessary, but not sufficient condition to achieve such monodispersed small particles. We can infer from Fig. 6.1 that the Pd-NP formation reaction by hydrazine oxidation may occur without kinetic hindrances at low and high pH. However, at pHs about 5, ΔE has a small (but positive) value, indicating according to Eq. (6.8) that the Pd-NP formation is thermodynamically driven but kinetically hindered. A similar argument cannot be given for the formation of Ag-NPs with hydrazine.

Another example of manipulation of redox potential with *p*H can be found in the article by Sánchez-Iglesias et al. [17]. These authors grew a Ag layer at room temperature through the reduction of Ag-ions with quinone/hydroquinone on a

Au-NP surface. The coupling of an acid–base equilibrium, allowed these authors to modify the hydroquinone redox potential with pH [18]. At a pH of 7.4 or higher, the hydroquinone redox potential is enough to reduce Ag, even if Au-NPs were present or absent. At pH values below 7 the redox potential becomes less negative and no reaction occurs even when Au-NPs are present. At intermediate pH values, it is possible to reduce Ag only on the Au-NPs surface.

Solvents play an important role on the NPs electrochemical synthesis [19]. These can play a multiple role on the preparation; for example, primary alcohols (methanol, ethanol) can work as solvent as well as reducing agents in the preparation of Pd, Pt and Au NPs, while the polyols (glycerol, diethylene glycol) can perform a triple function: as solvents, stabilizing and reducing agents, in the preparation of Cu and Ni NPs [20].

6.2.2 *Strong Versus Weak Reducing Agents*

The reducing agents that produce the metallic reduction reaction in Eq. (6.7) can be classified as weak or strong. However, as discussed in the previous section, this depends on the reaction conditions.

One of the most common reducing agents is hydroquinone (H_2Q). This agent is widely used for reducing Ag-ions for photo developing. In the photographic processing, the BrAg film exposed to light creates small Ag metallic clusters, which are too small to be visible with naked eyes. This constitutes what is commonly denominated as a photographic negative. The fogging process consists in provoking a growth in these metallic clusters through the addition of a solution containing H_2Q and additional Ag-ions. This makes the initial clusters grow until they become visible. H_2Q is incapable of reducing Ag-ions isolated in photographic film, but it is capable of reducing Ag-ions in the presence of pre-existent metallic clusters. Fayet et al. [21] proposed that these clusters should be composed of at least four atoms. The reason for this selection lies in its reduction potential. The energy used to reduce several Ag-ions to create a precursor seed is markedly different from the energy used to reduce ions on a pre-formed metallic cluster. This is the difference between homogeneous and heterogeneous nucleation, as we will discuss later. Table 6.2 shows estimates of the redox potential of different Ag metallic clusters [18]. From Table 6.2, we can observe that the hydroquinone redox potential is $E^0_{Q/H_2Q} = -0.7$ V for pH = 1 and it is incapable of exceeding the highly negative redox potential required to produce an isolated Ag atom, $E^0_{Ag^+/Ag^0_1} = 1.8$ V. However; it is enough to reduce Ag^+-ions if there are previously existing clusters made of four or more atoms, on which the redox potential for Ag^+ is $E^0_{Ag^+/Ag^0_4} = -0.4$ V or higher. It is worth mentioning that the Ag^+ ions could also be reduced on solid Ag, because $E^0_{Ag^+/Ag^0_\infty} = 0.8$ V. An analogous situation should occur in the formation of the Ag-NPs in solution.

Table 6.2 Redox Potential required to produce an Ag cluster of a given size

Redox system	E^0/V
$Ag^+ + e^- \rightarrow Ag_1^0$	−1.8
$Ag^+ + e^- + Ag_3^0 \rightarrow Ag_4^0$	−0.9
$Ag^+ + e^- + Ag_4^0 \rightarrow Ag_5^0$	−0.4
$Ag^+ + e^- + Ag_{\infty-1}^0 \rightarrow Ag_\infty^0$	0.799
$Q + 2H^+ + 2e^- \rightarrow H_2Q$	−0.699 (pH = 1)
$Q + 2H^+ + 2e^- \rightarrow H_2Q$	−0.3 (pH = 7)
$H_2BO_3^- + 5\,H_2O + 8e^- \rightarrow BH_4^- + 8\,OH^-$	−1.24 (pH = 14)
$C_6H_6O_6 + 2H^+ + 2e^- \rightarrow C_6H_8O_6$	0.13

Values taken from Ref. [18]

Borohydride $(BH_4)^-$ is one of the strongest reducing agents widely utilized in the generation of NPs and in many other applications in organic and inorganic chemistry. The redox potential, at pH = 14, is $E^0_{H_2BO_3^-/BH_4^-} = -1.24$ V. Borohydride reacts quickly with Ag^+-ions in solution to create Ag-NPs. Given its high reduction potential, this agent is used in the formation of initial clusters of almost all transition metals. In the particular case of Ag, and when observing the reduction potentials shown in Table 6.2, it seems contradictory that the $(BH_4)^-$ may reduce Ag^+-ions. Nevertheless, it should be taken into consideration that in general, for a reaction to take place in solution, the Ag^+-ions are complexed, a fact that reduces the free energy necessary (or the potential) to form the precursor seed, as it can be observed in Table 6.1. To thoroughly analyze this problem, we can resort to the experiment by Gentry et al. [18], whose results are represented in Fig. 6.2. There, we see the absorption spectra for Ag nanoparticles grown using as reducing agents (a) H_2Q and (b) $(BH_4)^-/H_2Q$. Figure 6.2a shows the spectrum when the solution containing Ag-ions is exposed to reduction of H_2Q; no formation reaction is observed. On the contrary, when $(BH_4)^-$ is added to the electrolyte solution, Ag-ion reduction starts and a shoulder near 400 nm (Fig. 6.2b) starts to appear in the absorption spectrum. After the whole $(BH_4)^-$ has reacted, then authors proceed to add H_2Q observing an increase in the absorption spectrum intensity, thus indicating the growth of the Ag-NPs previously formed (Fig. 6.2b). In other words, H_2Q is useful as a weak reducing agent (incapable of forming initially Ag) once a strong reducing agent such as $(BH_4)^-$ is employed to start the formation process. A similar discussion is valid with stronger and weaker reducing agents other than borohydride and hydroquinone.

6.2.3 Formation Mechanism of Monoatomic Nanoparticles

Metallic atoms generated by reduction according to Eq. (6.7) are substantially insoluble in aqueous media and, therefore, they become gradually added in groups called embryos. Embryos are dynamic entities that intervene in the process of

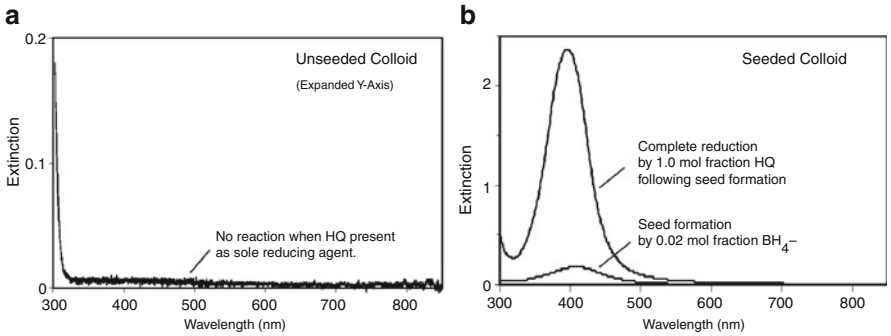

Fig. 6.2 Extinction spectra on (**a**) unseeded and (**b**) seeded samples. The unseeded colloid contained 1.0 mol fraction HQ relative to the number of moles of $AgNO_3$, but no $NaBH_4$. The seeded colloid was initially charged with 0.02 mol fraction $NaBH_4$. HQ (6.0 mol fraction) was added to the seeded sample after 3 min. All samples contained 0.2 mM $AgNO_3$ and 0.2 mM sodium citrate (Reprinted with permission from Ref. [18])

continuous dissociation-condensation. As new metallic atoms are generated, embryos grow until they reach a determined size, called precursor seed. The nuclei size depends on several reaction parameters such as the solubility constants, solute concentration, redox potential, temperature, nature, and concentration of surfactants, of solvent viscosity and surface tension. These nuclei are, as a rule, metastable since they represent a system of relatively large free energy. These nuclei can grow through two different mechanisms: reduction of material on the seed surface and through addition of other nuclei in themselves. To produce NPs of practically the same size (monodispersity), the coalescence process among nuclei must be hindered at the early stages. This objective can be fulfilled by manipulating the electrostatic and/or steric effects of each NP. Electrostatic stabilization, strictly based on manipulating the equilibrium between attractive and repulsive forces, has little impact on the concentrated systems. There, the double layer is compressed due to the high ionic strength and, consequently, the NPs can get closer and undergo aggregation. By contrast, in dilute systems, the impact of the double layer is quite effective and has the advantage of leading to stable dispersions because the extension of the double layer is large. Electrostatic stabilization consists in the adsorption of surfactant, polymers, or polyelectrolytes, which counterbalances the van der Waals forces. The efficiency of both types of hindrance significantly depends on the system under study.

Let us consider for simplicity the free energy of formation of a monoatomic, naked, free-standing nanoparticle at an overpotential η, which is given by:

$$\Delta\widetilde{G}^{\text{form}} = \left[G^{\text{NP}} - N_{\text{M}}\mu_{\text{M}}^{\text{bulk}}\right] + ze_0N_{\text{M}}\eta \tag{6.9}$$

where G^{NP} is the free energy of the NP, N_{M} is the number of its constituent atoms, and $\mu_{\text{M}}^{\text{bulk}}$ is the chemical potential of the atoms in the bulk metal, since we are

considering this material as the reference. Following Eq. (6.2), at first approximation, $\left[G^{NP} - N_M \mu_M^{bulk}\right]$ term is positive and proportional to the number of surface atoms, so $\left[G^{NP} - N_M \mu_M^{bulk}\right] \approx \alpha N_M^{2/3}$. Then Eq. (6.9) may be approximated by:

$$\Delta\widetilde{G} = \alpha N_M^{2/3} + z e_0 N_M \eta \tag{6.10}$$

This equation has been widely used to analyze nucleation and growth phenomena. Note that the first chemical term is proportional to $N_M^{2/3}$ and the second one, the electrochemical term, is proportional to N_M. Thus, the electrochemical factor has a larger power dependence in $\Delta\widetilde{G}$ than the surface term and the former will predominate in the limit $N_M \to \infty$. Thus, the behavior of $\Delta\widetilde{G}$ will be of two different types, depending on whether $\eta > 0$ or $\eta < 0$. This situation is illustrated in Fig. 6.3.

In the first case, $\eta > 0$, the electrochemical factor will add the monotonic growing function $z e_0 N_M$ to the surface energy term, so that $\Delta\widetilde{G}$ becomes always positive for all N_M. This behavior is the natural consequence of the increasing area of the growing NPs, and shows that, subject to the chemical potential of the bulk metal M, particles of all sizes will tend to dissolve.

In the second case, where $\eta < 0$, the electrochemical contribution will add a monotonic decreasing term to the monotonic increasing surface term, so that a maximum will appear at $N_M = N_M^*$, corresponding to the critical cluster size. This situation is illustrated qualitatively in the broken line of Fig. 6.3, and corresponds to systems where the thermodynamic stable state is the bulk material. Particles of size N_M^* are in an unstable equilibrium. Smaller particles will dissolve, and larger particles will grow towards the bulk condition. The application of a more negative overpotential, $\eta << 0$, shifts N_M^* to lower values, but the maximum still persists.

Figure 6.4 shows the energetic contribution to $\Delta\widetilde{G}$ for the growth of an Au-NPs with two different crystalline structures, as obtained from computer simulation based on semiempirical embedded atom potentials [22–24]. It can be observed that the overall behavior is qualitatively similar to that described in Fig. 6.3 and

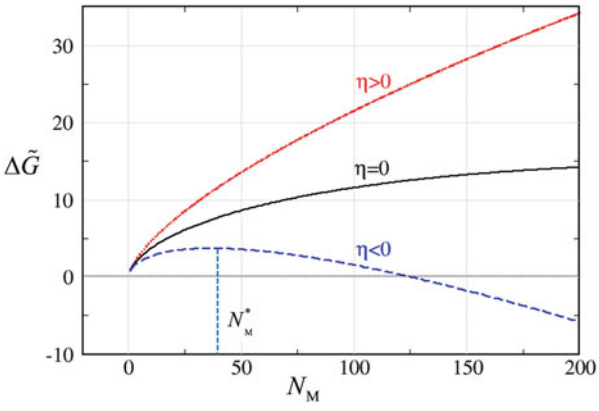

Fig. 6.3 Qualitative scheme of the excess of Gibbs energy, $\Delta\widetilde{G}$, as a function of the number of atoms of the NP, N_M. Note the monotonically growing behavior for $\eta > 0$ and the occurrence of a maximum for $\eta < 0$, corresponding to an unstable state

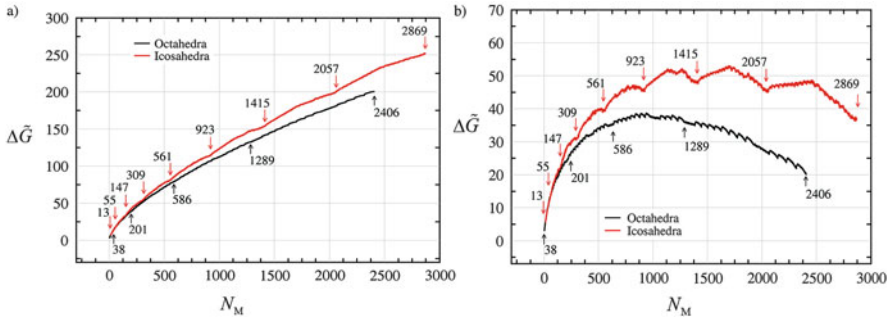

Fig. 6.4 Potential energy excess as a function of the number of atoms N_M for octahedral (*black lines*) and icosahedral (*red lines*) Au nanoparticles. The plots correspond to overpotentials of (**a**) $\eta = 0$ and (**b**) $ze_0\eta = -75$ mV. Some selected numbers of atoms, corresponding to closed shells, are marked with *arrows*

Eq. (6.9). However, the presence of a crystalline structure generates a sawtooth behavior of the curve, something that is characteristic of this type of systems [25, 26]. While the minima marked by arrows in Fig. 6.4 correspond to the completion of full shells in the NP, the fine structure is due to growth of individual facets. The latter are a consequence of the local minimization method employed in [27, 28] and could disappear if global optimitization methods are used [3]. The layer-by-layer growth characteristic of these metastable systems [7, 27], may be understood in terms of the presence of local minima, separated by barriers of the order of the eV, we will later return to this issue. The beginning of crystal growth (nucleation) takes place under supersaturation conditions. That is, the electrochemical potential of the metal ions must be larger than that corresponding to the bulk phase ($\eta < 0$). Under supersaturation conditions any NP size is unstable and, consequently, the NP should grow ad infinitum or dissolve. This "grand canonical" picture (in the sense of an open system) of NP growth actually occurs in the synthesis in a rather short period of time. As the NP grows, the concentration of ions in solution starts to decrease, the system approaches equilibrium and subsequently the $\mu_M^{NP} \rightarrow \mu_M^{bulk}$. The later conditions correspond to a rather "canonical" picture of growth. Both pictures regarding NP growth coexist in the literature. As it will be further seen, a canonical view is useful to understand the processes of nucleation and growth, while a grand canonical view allows understanding stabilities in the processes of NP formation via upd.

A consequence of the fact that $\mu_M^{NP} > \mu_M^{bulk}$, making the NP unstable with respect to the bulk material, is that most of the methods of NP synthesis must control their size and morphology using kinetic strategies to block their growth. In order to understand this, a scheme was proposed by LaMer in the 1950s [28] and it is known as the "burst nucleation" concept. As it was mentioned in the above paragraphs, most of the methods employed in the formation of NPs require a supersaturation to proceed. In this process, many nuclei are generated at the same time, and then these nuclei start to grow. Because all of the particles nucleate almost simultaneously,

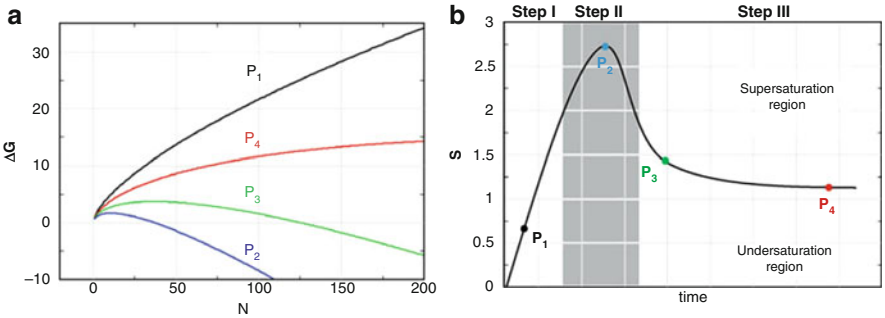

Fig. 6.5 (**a**) Typical free energy profile for the growth of a NP according to Eq. (6.9). (**b**) LaMer plot, change of saturation as a function of reaction time

their growth histories are nearly the same. This is the essence of the "burst-nucleation" process, which makes it possible to control the size distribution of the ensemble of NPs as a whole during growth. "Burst nucleation" has been adopted as an important concept in the synthesis of monodisperse NPs. As a synthetic strategy, this method is often referred to as "the separation of nucleation and growth". In this homogeneous nucleation process, there exists a high free energy barrier, mainly due to the appearance of a new interface between the new (growing) phase and the original one (precursor).

How does burst nucleation work? At a given moment, the precursor agent starts to be injected. Let us further assume that diffusion is infinitely fast, so that matter is uniformly dispersed all over the volume of the system, and that its temperature remains unchanged. As the initial concentration of precursor is small, $\mu_{\mathrm{M}}^{\mathrm{NP}} > \mu_{\mathrm{M}_{(\mathrm{aq})}^{z+}}$, where $\mu_{\mathrm{M}_{(\mathrm{aq})}^{z+}}$ is the chemical potential of M^{z+} in solution. A typical point in this region would be for example point P1 in Fig. 6.5b. The work of nucleation should be similar to that described in curve P1 in Fig. 6.5a. This condition is generally called subsaturation region. Upon further addition of matter, $\mu_{\mathrm{M}}^{\mathrm{NP}} < \mu_{\mathrm{M}_{(\mathrm{aq})}^{z+}}$, locating the system in the supersaturation region. Supersaturation increases continuously until the injection of matter stops. This point corresponds to step II, called "the nucleation stage". At this moment, the amount of metallic precursor is maximal, so that metal activity and the solubility coefficient take their largest value. This corresponds to the point marked as P2 in Fig. 6.5b. The work of nucleation under these conditions will look like the curve P2 in Fig. 6.5a. At this time, the critical nucleus size reaches its lowest value. As the system is under supersaturation conditions, very frequently growth nuclei are formed; many of them being unstable, but occasionally large fluctuations are produced so that these fluctuations overcome the above-mentioned critical nuclei. These NPs are stable and begin their growth. At the same time these nuclei grow, other new nuclei are formed, and the precursor concentration drastically decreases. The situation at this intermediate period is for example that of point P3 in Fig. 6.5b, and its work of nucleation is described by curve P3 in Fig. 6.5a. In LaMer's curves, this corresponds to the third stage of the

process, and the latter is generally called the "growth stage". When the precursor concentration decreases, the critical nucleus size displaces toward larger values. At this stage, the probability of nucleation is relatively low. This prevents the formation of new nuclei and favors the growth of those already existing. Growth continues and μ_M^{NP} decreases asymptotically to $\mu_{M_{(aq)}^{z+}}$. At this moment, the critical nucleus size has reached a very large value; a typical point for this situation has been marked as P4 in Fig. 6.5a, b. At this stage, the nucleation process is practically suppressed and only the growth of nucleus previously formed is observed. The experiment described above is the essence of the separation between the nucleation and growth processes. As the transition time between stages I and II becomes faster, the monodispersity of the NPs formed increases.

In systems with a rather low speed of metal reduction, the formed nuclei can fluctuate between crystal structures and twined crystals [29]. This frequency of structural exchanges decreases when the NP size increases, until the point in which the NPs are trapped in one of these structures. These structures will serve as a guide for growth. Many applications need to be able to select some of these structures. A solution to this may be including new components to the system, which allow differentiating them even more in energy and finding a way to separate selectively nuclei from each other to obtain a better monodispersity of the NPs structures synthesized. For example, this is the case of adding to the reactants small quantities of oxygen and chloride ions to select the Ag-NP type to be obtained. In presence of these two components, the twinned structures can be dissolved because the twinning sites provide active sites for NP oxidation (little coordination). This corresponds to an etching process, where chloride acts as a coordinator causing also oxidation of these sites. As a result, the final NPs present only crystal structures with {111} and {100} type facets [30].

The differences between theoretical predictions and experimental results suggest that the nucleation process of NPs in aqueous solution does not proceed via the classical pathway from LaMer's point of view; but it follows ways that are more complex and it involve several steps. For example, little nuclei can be linked together to form bigger and more stable nuclei. In order to understand this phenomenon, two models have been proposed: the Lifshitz-Slyozov-Wagner model [31, 32] and the two-stage model [33]. There is evidence that clusters of smaller sizes than the critical one, are sufficiently stable to the extent that successive aggregation of these units cause a rise in the speed of NPs formation [34]. The interaction (coordination) between solvent and/or surfactants molecules with small clusters can stabilize the molecules enough time so that these little units can be added to form a single big group, which eventually nucleates towards the bulk phase. Then, the presence of other components in the thermodynamic formulations is necessary to allow analyzing the effect of anions, solvents, surfactants, and so on. Important advances on the influence of these contributions on the formation of upd monolayers have been the pivot of the discussion in Chap. 3 of the present book. However, its extrapolation to the nanoscale still corresponds to a vacant issue in current literature.

6.2.4 Statistical Mechanic Formulation on the Stability and Metastability of Nanoparticles

In the present Section we will focus on the problem of stability of homoatomic nanosystems, with the aim of extending later these concepts to the study of upd on nanoparticles. To this purpose, we will use the Hill and Chamberlin model (HC) [35] originally developed to study the conversion of metastable (nanometric) drops of a liquid into its bulk phase. Important similarities arise for the formation of NPs in solution. This formalism was based on nanothermodynamics rules. For an introductory view, we address the readers to the first chapter of Hill's book on small systems [36].

The partition function of an incompressible, completely open system may be written as follows:

$$\Upsilon(\mu, T) = \sum_{N_M=1}^{\infty} Q(N_M, T)\exp[\mu N_M / k_B T] \tag{6.11}$$

where $Q(N_M, T)$ corresponds to the canonical partition function of an N-atoms sized cluster at temperature T. If we further consider that the system is made of a spherical cluster, $Q(N_M, T)$ takes the form:

$$Q(\mu, T) = c(T) N_M^4 \exp\left[-\alpha(T) N_M^{2/3} + \mu_M^{bulk} N_M / k_B T\right] \tag{6.12}$$

The term $c(T)N_M^4$ corresponds to rotational and translational contributions, $\alpha(T)$ is proportional to the surface tension and the term $\mu_M^{bulk} N_M / k_B T$ is related to the partition function of N_M particles in the bulk. Replacing Eq. (6.12) into Eq. (6.11) yields:

$$\Upsilon(\mu, T) = c(T) \sum_{N_M=1}^{\infty} N_M^4 \exp\left[-\left(\varphi N_M + \alpha(T) N_M^{2/3}\right)\right] \tag{6.13}$$

where the coefficient of saturation has been defined as $\varphi = \left(\mu_M^{bulk} - \mu\right)/k_B T$. If $\varphi > 0$ the system is in a subsaturation region; if $\varphi < 0$ it is in supersaturation conditions. If $\varphi = 0$ the system is right at the saturation limit. The probability density of observing a cluster made of N atoms may be written as follows:

$$P_{N_M}(\mu, T) = \frac{c(T) N_M^4 \exp\left[-\left(\varphi N_M + \alpha(T) N_M^{2/3}\right)\right]}{\Upsilon(\mu, T)} \tag{6.14}$$

The main idea in the HC model is to analyze stability in terms of the numerator of $P_{N_M}(\mu, T)$, since $\Upsilon(\mu, T)$ is fixed for the given μ and T. Then, a plot of $f(N_M, \mu, T)$

defined as $f(N_M, \mu, T) = P_{N_M}(\mu, T)\Upsilon(\mu, T)$ will present the same behavior as $P_{N_M}(\mu, T)$ out of a constant factor. A more suitable form to represent f is to make the changes of variables $n = \alpha^{3/2} N_M$ and $\delta = \alpha^{-3/2}\varphi$, to get:

$$f(N_M, \mu, T) = f(n) = n^4 \exp[-\delta n] \exp\left[-n^{2/3}\right] \tag{6.15}$$

Figure 6.6a shows a contour plot of $f(n)$ as a function of δ and $\log(n)$ at 300 K. We have selected four representative iso-saturation lines to this purpose: $\delta = 0$, -0.04, -0.07, and -0.09, which are plotted in Fig. 6.6b–e. Each of the factors in Eq. (6.15) has been marked in Fig. 6.6b–e to illustrate the different contributions to $f(n)$. We can mention that the surface component is always a decreasing quantity (green curve), and that its value depends on the surface energy of the NP being formed. The rotational-translational contribution (red curves) is always a monotonically increasing function. The product of the two former components (the case of $\delta = 0$, black curve) determines a maximum of $f(n)$ around $\log(n) \approx 2.6$ (Fig. 6.6b). This maximum indicates a finite probability of finding nanoclusters of a given size at $\delta = 0$ and it is a consequence of the rotational-translational contribution. Turning into our focus of interest, that is, metallic NPs, the previous results a rather awkward prediction, since this would mean the occurrence of stable NPs at zero overpotential. On the contrary, we are aware from experiment that always overpotential is required for the growth of a new phase, to overcome the critical nucleus size, as analyzed above in Fig. 6.3. One of the points to be considered is that the traditional electrochemical conditions are usually not with free-standing NPs but deposited on a substrate, where the rotational-translational contribution, responsible for the maximum in Fig. 6.7b, vanishes. The other point to consider is the magnitude of the parameter α. An estimation of α yields in the range of $31 < \alpha < 57$ and $53 < \alpha < 55$ at room temperature for Au and Ag, respectively [38]. So the "drop" size would yield between $7 < N_{Au} < 13$ and $N_{Ag} \approx 8$, that is, very small values. It must be emphasized that such a prediction is absent in the formulation leading to Fig. 6.3, where the rotational-translational considerations were absent. At moderate supersaturation conditions, for example $\delta = -0.04$, the term containing the chemical potential (blue curve) starts to be noticeable, and the maximum of $f(n)$ is shifted towards larger n values, while its value increases (see Fig. 6.6c). At larger supersaturations, for example $\delta = -0.07$, Fig. 6.6d, the behavior remains the same and a steep increase is found in $f(n)$ above $\log(n) \approx 7$. This sudden increase in $f(n)$ after the maximum denotes the mathematical divergence of the probability density for $n \to \infty$, because of the fact that the supersaturation term is dominating the probability density for large nanodrop sizes. This divergence is associated to the occurrence of the bulk phase.

In Fig. 6.6d, it can be noted that in the region $5.7 < \log(n) < 7$ the probability density of finding a nanocluster is practically negligible. This area of low probability acts as a bottleneck for the transition of n-sized drops towards the bulk phase. However, this situation reaches a limit at larger supersaturations. For example,

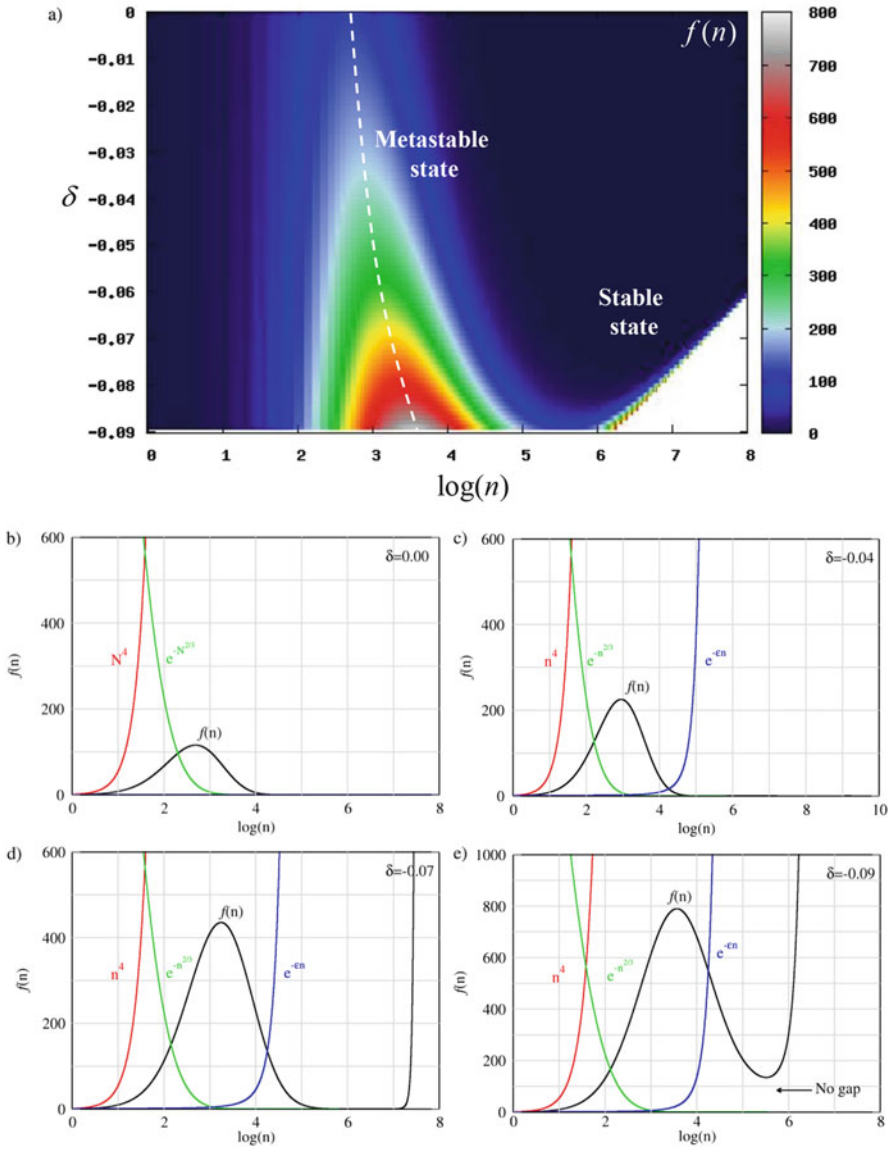

Fig. 6.6 (**a**) Contour plot of the function $f(n)$ at a constant temperature. Contributions of the different factors in Eq. (2.10) at diverse values of the normalized supersaturation δ. (**b**) $\delta = 0$, (**c**) $\delta = -0.04$, (**d**) $\delta = -0.07$, and (**e**) $\delta = -0.09$. In (**b**–**e**) the *green curve* has been multiplied by a factor 10^4 to fit into scale. See discussion in the text

Fig. 6.6e shows that at $\delta = -0.09$ the region where $f(n) \sim 0$ has disappeared, and it can be expected that small fluctuations, even of one particle, may lead to the transition to the bulk liquid. At very large supersaturations (not shown here), the

metastable nanocluster should no longer be observed, remaining only a monotonic growth towards the bulk phase. In Fig. 6.6a it can be observed how the region corresponding to the bottleneck progressively becomes thinner with increasing supersaturation. The rate at which the steep increase in $f(n)$ moves towards small n for decreasing δ is larger than the rate at which the metastable state moves towards large n. White broken lines in Fig. 6.6a represent this. The broken line on the left shows the position of $f(n)$ maximum, while the broken line on the right shows the evolution of a point at which $f(n) = 10^3$. Although the two lines have not converged into a representative point in the region analyzed in Fig. 6.6a, it can be seen that the dark blue region (bottleneck), i.e., the one with a negligible probability, has disappeared for $\delta = -0.09$, so that the system will no longer be confined to a metastable state at this supersaturation value.

The bottleneck in Fig. 6.6 represents a kinetic hindrance for the phase transition under consideration. The size of the gap may be related to an activation energy [39], in the sense that if this activation energy is large enough (wide probability gap), the transition will not take place at the timescale of experiment. This "confination" allows the computation of the thermodynamic properties of the nanoclusters, even when their structures do not correspond to a global minimum of the free energy of the system.

The idea of what Hill and Chamberlin called physical convergence of the probability density emerged from the previous analysis [25]. When the mathematical divergence is shifted onto large drop sizes ($\delta \to 0^-$, to denote that we are approaching the zero from small negative values), and we are interested in the calculation of properties of the metastable NP, the sum in Eq. (6.13) may be truncated to give:

$$\Upsilon(\mu, T) = c(T) \sum_{N_M=1}^{N_0} N_M^4 \exp\left[-\left(\varphi N_M + \alpha(T) N_M^{2/3}\right)\right] \tag{6.16}$$

where N_0 corresponds to a value of N at the minimum of the argument of the sum. Please note that $N_0 = N_0(\mu, T)$ is a function of chemical potential and temperature. As it is always the case, knowledge of the partition function allows calculation of all properties related to the metastable nanocluster.

When the system is in undersaturation conditions ($\delta > 0$), no divergence is found in the probability density, since under these conditions the sum (6.16) always converges. At moderate undersaturations ($\delta \to 0^+$, to denote that we are approaching the zero from small positive values), $f(n)$ presents a maximum and the nanocluster properties may be evaluated straightforwardly, since the local maximum in $f(n)$ is also a global one. Despite the simplicity of the model, Hill and Chamberlin showed that just at the saturation point (and at small subsaturation coefficients), clusters can be thermodynamically stable. That means that a supersaturation is not necessary to form initial clusters. Rotational and translational contributions are responsible for this "extra stability" not considered in Eq. (6.10).

6.2.5 *Bimetallic Nanoparticles*

Preparation of bimetallic NPs, from its precursors, is relatively more complex than the homoatomic synthesis. In general terms, this can be divided into two alternatives: a co-reduction or a successive reduction.

Co-reduction is the simplest method, where two or more precursors are simultaneously reduced. Morphology and space distribution of species within the NP, mainly depend on the velocity constants of the NP intrinsic processes: reduction potentials, self-diffusion, exchanges, etc. When the redox potentials of the two metals are similar, ($E_1^0 \sim E_2^0$) and ΔE is big (see Eq. (6.8), predominantly alloyed NPs are obtained [40, 41]. When the redox potentials of the two metals are different and are moderately big, the metallic species with the higher redox potential will precipitate first, forming the NP nucleus, followed by co-solubility of the second component, which prevails on the surface. It is worth mentioning that the solubility sequence can be reverted by the formation of complexes with ligands that creates a complex significantly stronger with the core formation metal. For example, in Fig. 6.1 it can be observed that Pd oxidizes at a more positive potential than Ag, so that attempt of reduction of both materials under similar conditions should prioritize mainly a core of Pd and an external layer rich in Ag. Nevertheless; when ammonia is added to the solution (at a relatively high pH), the reduction potentials are inverted, modifying the reduction priorities. In this last case, we should expect a core rich in Ag and a Pd shell.

In the *successive reduction* method, each reduction stage is carried out in different periods. The second reduction is carried out on the pre-formed NP surface (called seed-NP). This kind of growth implies a second nucleation stage. The temporary phase-lag of the stages is special for the NP posterior growth or the formation of core@shell NP. This kind of growth mechanism has been known from the beginning of the last century. It has also been used for the growth of homoatomic NPs as well as for bimetallic ones [42, 43]. We will discuss this kind of deposition in Sect. 6.4, where a model to describe the stability of preformed NPs will be set out.

Getting into the electrochemical field, it comes out that various strategies, originally used for the modification of flat surfaces, are nowadays successfully applied to design and modify nano-sized structures. Among these, it is of great interest the modification of a metal surface by upd, which as discussed in previous chapters consists in metal deposition on a foreign substrate at potentials positive with respect to the Nernst thermodynamic prediction. The potential utility of upd is due to the relatively rapid, simple, and precise modification of the reaction conditions, which allow controlling the degree of coverage of the adsorbate metal on the substrate surface. The main obstacle to the implementation of upd for a large number of systems is the fact that this phenomenon is usually limited to the deposition of a less noble metal on a nobler one. In the case of electrocatalytic applications, this situation is right the opposite to the desired one. One way to circumvent this problem is to use a technique denominated galvanic replacement

(gr). In this method, the substitution of a sacrificial upd sub/monolayer by the desired noble metal atop in circuit allows to obtain the desired catalyst. Applied together, upd and gr allow reducing the quantity of noble metal used to a minimum amount, thus reducing the economic costs of the final product. This is a key objective for potential industrial applications. Thus, both upd and gr appear as attractive bottom-up methods, with great prospects for the development of novel nanomaterials. Upd and gr are considered particular types of successive reduction methods.[1]

6.2.6 *Deposition Mechanisms at the Nanoscale*

In analogy with metallic deposition mechanisms on planar surfaces [44], three types of growth at the nanoscale have been described:

- "Volmer-Weber" or three-dimensional island growth,
- "Frank-van der Merwe" or layer-by-layer growth,
- "Stranski-Krastanov" or three-dimensional island growth on a pre-formed layer.

In the first mechanism, the binding energy between the adsorbate and the substrate is smaller in absolute value than the binding energy of the native metal. This type of growth is common in systems presenting overpotential deposition (opd). In the second and third mechanisms the binding energy between the adsorbate and the substrate is larger than the binding energy of the native metal. Thus, two-dimensional phases can be formed driven by this magnitude. These growth types are typical of systems presenting upd. The difference between the second and the third growth types lays in the crystallographic mismatch between the adsorbate and the parameters of the substrate. For systems displaying a fairly small difference between their lattice parameters, it is expected that they follow a layer-by-layer growth type. On the other hand, for systems displaying a fairly large difference between their network parameters, it is expected that they follow the Stranski-Krastanov mechanism. As the number of deposited layers increases, a tension (caused by the crystallographic mismatch) accumulates so that the shell breaks on top and the growth method changes from layer-by-layer to three-dimensional island growth. Clearly, this division of growth mechanisms is a rather simplified picture of the real situation. It is well known that for a NP of a single material, the lattice parameter of the subsequent layers composing the NP varies according to size. The definition of crystallographic mismatch, as it is taken from flat surfaces makes no sense; at the nanoscale, this parameter is function of size. These deformations generate instability. There are two types of instabilities at the nanoscale [45]. The first one is that produced inherently by the geometry of the NP, which may deviate in its inner structure from that expected for the bulk material. This is for example

[1] See discussion on Sect. 7.1 in Chap. 7.

the occurrence of icosahedral structures in the case of metals with bulk *fcc* structure. This instability increases when the number of the layers of the nanoparticle grows. The second type of instability appears in the case of substrate/adsorbate systems, where the lattice mismatch between the adsorbate and the substrate leads to the Stranski-Krastanov growth type.

6.3 Towards Electrochemical Control in Synthetic Routines for Free-Standing Nanoparticles

In the early 2000s, detailed electrochemical studies on nanoparticles were carried out by Park and Weaver [37, 46], who investigated by voltammetric experiments the upd of Cu on Au NPs of different sizes. Figure 6.7a schematically shows Park and Weaver experimental design [37, 46]. Here, the NPs are placed above a conductive film that is in contact with the electrolytic solution containing ions Cu^{+2}; the NPs surface potential was controlled by a potentiostat. Figure 6.8a shows the voltamperometric profile obtained for the deposition of Cu on 13 nm-in-diameter NPs (solid trace) in the presence of sulfate ions. Cathodic and anodic sweeps show the presence of two pairs of reversible processes, a-a′ and b-b′, associated with the electrodeposition of upd-Cu and of bulk Cu (see also Fig. 6.8). The curve represented in a dotted line corresponds to the potential sweep in the absence of NPs, thus indicating that the conductive film is not permeable to Cu^{+2} ions. So, these authors concluded that the measured current is produced only by the reduction of Cu^{+2} on Au NPs.

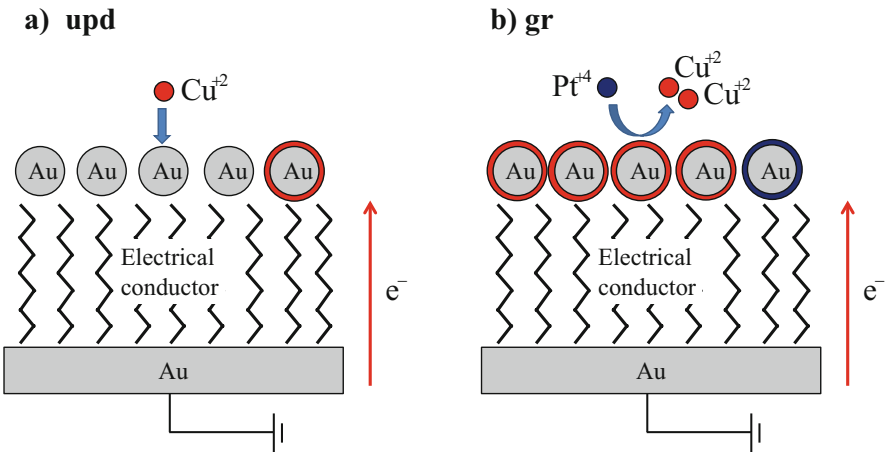

Fig. 6.7 Schematic representation of the process used by Park and Weaver to produce core@shell NPs of Au@Cu and Au@Pt using (**a**) underpotential deposition and (**b**) underpotential deposition in conjunction with galvanic replacement (Adapted with permission from Ref. [37])

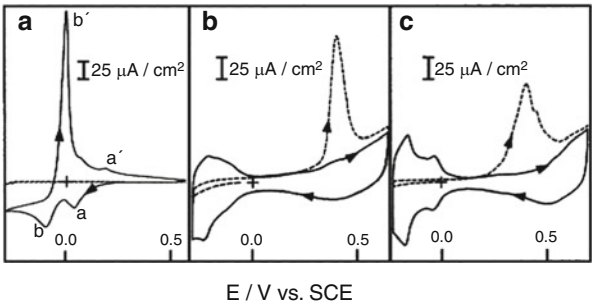

Fig. 6.8 Voltammograms (**a**) at (5 mV s^{-1}) for Cu deposition on Au-NPs ($d_{NP} \approx 13$ nm) in 0.1 M $H_2SO_4 + 1$ mM $CuSO_4$ (*Solid trace*). Baseline (*dashed trace*) was obtained in the absence of Au-NPs. (**b**) *Solid trace*: cyclic voltammogram (50 mV s^{-1}) for Pt modified Au-NPs in 0.05 M H_2SO_4; *dashed trace* is for electrooxidation of irreversibly adsorbed CO. (**c**) Similarly to (**b**), but for Pt-NPs ($d_{NP} \approx 6$ nm) in absence and presence of a CO adlayer (Reprinted with permission from Ref. [37])

Similarly, Fig. 6.7b shows a scheme of the model used by Park and Weaver in Reference [37] for the fabrication of Au@Pt NPs using Cu upd and subsequent galvanic replacement of the upd deposit by Pt^{4+}. Figure 6.8b shows the voltammogram for Au@Pt NPs in absence (continuous curve) and in the presence (dotted lines) of CO. The current peak in the dotted line curve appearing between 0.4 and 0.5 V corresponds to the CO irreversible electrooxidation characteristic for Pt surfaces. Figure 6.8c shows the voltammogram for Pt NPs of 6 nm diameter, in the presence and absence of CO. The comparison of Fig. 6.8b, c shows that the electrochemical behavior, concerning CO electrooxidation, of the Au@Pt core-shell is similar to that of pure Pt.

In a different approach, Zhang et al. and Lu et al. [47, 48] presented a synthesis protocol where the electrons needed for the metallic reduction process are released by a molecule which is in solution, see Fig. 6.9a, thus avoiding the use of a potentiostat as electrons source. These authors seeded Au-NPs of 12 nm diameter on graphitic carbon (GC) and grew a Pt layer on the surface of the Au-NPs using ascorbic acid as reducing agent.

The reduction equation that represents this growth is:

$$Pt^{4+} + Au_{NP}/GC + 4e^- \rightarrow Au_{NP} @ Pt/GC$$

where electrons are provided by the oxidation reaction of ascorbic acid. Figure 6.9b shows cyclic voltammograms obtained with 12 nm diameter Au NPs and Au@Pt NPs, both deposited on GC. The Au-NPs/GC electrode shows the electrochemical behavior of a typical Au electrode. However, when substituted by a Au(core)@Pt(Shell)/GC system, the CVs resemble the one of a pure Pt electrode. This can be visualized in the CV in the characteristic peaks of hydrogen adsorption/desorption between −0.3 and +0.1 V, as well as in platinum oxide formation and reduction at higher potentials. The absence of the peak corresponding the

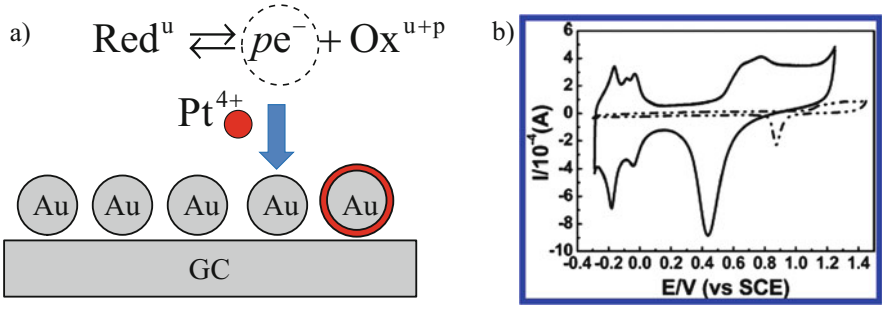

Fig. 6.9 (**a**) Schematic representation of the process of NP formation of core@shell type using molecules with redox activity as reducing agent. (**b**) Cyclic voltammogram (50 mV/s) corresponding to Au NPs of 12 nm (*dotted line*) and Au(core)@Pt(shell) NPs of 50–60 nm in 0.5 M of H_2SO_4 (Reprinted with permission from Ref. [47])

Au oxidation ($\sim$ 0.9 V) indicates that the Au cores are completely covered by Pt. Pt deposition on Au surfaces is a typical system with opd growth. Consequently, in Zhang´s et al. experiment previously described, it is not possible to control the thickness of the Pt layer thermodynamically. These authors obtained a Pt layer between 38 and 48 nm thick. It should be noticed that in this type of experiments the potential (fixed by the reductant, here ascorbic acid) may be considered as constant during all the reaction. Thus, Zhang´s experiment can be compared with an electrochemical growth at a constant potential in the overpotential region.

Selvakannan et al. [15] showed that tyrosine can be used as reducing agent in alkaline conditions, to reduce Ag^+ ions on the surface of Au-NPs without the need of a support. The reduction process of the Ag^+ ions can be represented as follows:

$$Ag^+ + Au_{NP} + e^- \rightarrow Au_{NP} @ Ag$$

where $Au_{NP}@Ag$ denotes a free standing NP in solution. The electrons necessary for the reduction process come from the oxidation of tyrosine, according to the following oxidation reaction:

$$Tyr^- \rightarrow \text{semi-quinine} + e^-$$

in which semi-quinine refers to the structure obtained after tyrosine oxidation. The global electrochemical equation is:

$$Ag^+ + Au_{NP} + Tyr^- \rightarrow Au_{NP} @ Ag + \text{semi-quinone}$$

Tyrosine presents acid–base activity:

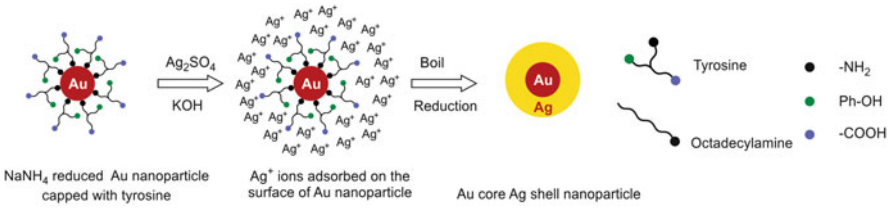

Fig. 6.10 Formation scheme of a core-shell Au@Ag NP according to Selvakannan´s method (Reprinted with permission from Ref. [15])

$$\mathrm{Tyr} \leftrightarrows \mathrm{Tyr}^- + \mathrm{H}^+$$

where we note that the species which causes the Ag reduction reaction is Tyr^- but not Tyr. At high pH values the ionization of the tyrosine phenolic group is produced, leading to a semi-quinone structure. Figure 6.10 shows the NPs formation scheme by Selvakannan method [15].

At intermediate or acid *p*H values, this ionization is hindered and consequently Ag reduction does not take place. Thus, the *p*H of the solution was used as a switch (on/off), to control the occurrence of the reaction. Other amino acids such as tryptophan and aspartic acid, allow the reduction of Au ions, but do not allow the reduction of Ag^+ ions [49, 50].

Fonticelli et al. showed in 2007 [51] that p-benzoquinone (a molecule with similar characteristics to those of tyrosine) can be used to reduce Ag^+ ions on the surface of a Au-NP coated with thiol molecules. The main difference between the experiments of Selvakannan et al. and those of Fonticelli et al. is that in the first case, the reducing molecules were on the surface of the NP while in the second, they were free in solution. This is a slight but significant difference, since the reducing molecules on the surface of the NP may be influenced by the presence of a second material, thereby affecting the deposition process.

The equation of oxidation for the reducing agent in the case of Fonticelli et al. is:

$$\mathrm{QH_2} \leftrightarrows \mathrm{Q} + 2\mathrm{H}^+ + 2\mathrm{e}^-$$

in which QH_2 and Q represent p-benzoquinone and p-hydroquinone, respectively. The equilibrium potential (Nernst) of the couple is:

$$E^{\mathrm{r}}_{\mathrm{Q/QH_2}} = E^{0}_{\mathrm{Q/QH_2}} + \frac{RT}{2F}\ln\left(\frac{a_{\mathrm{Q}}a^2_{\mathrm{H}^+}}{a_{\mathrm{QH_2}}}\right)$$

in which $E^{0}_{\mathrm{Q/QH_2}} = 0.6992$ V vs NHE is the standard potential of the couple. It is clear that $E^{\mathrm{r}}_{\mathrm{Q/QH_2}}$ is a function of pH, as illustrated in the inset of Fig. 6.11b. If the *p*H of the solution is selected lower than 1, the deposition potential (controlled by the redox couple) is moved to more positive values than the Ag bulk deposition

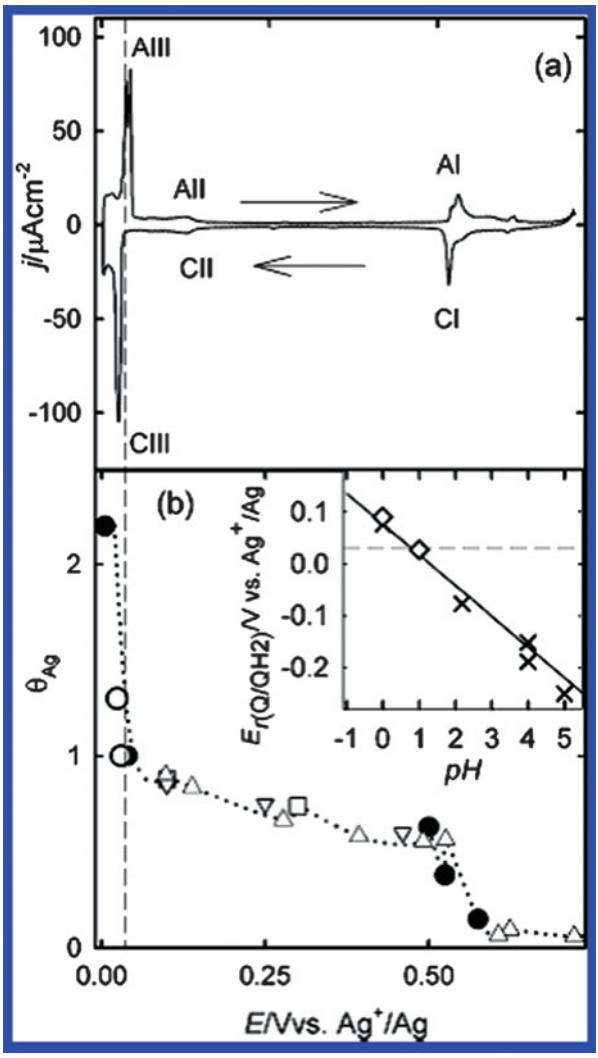

Fig. 6.11 (**a**) voltammogram for Ag deposition on the surface of Au(111) (**b**) θ_{Ag} vs. E plot obtained from different data. Circles correspond to coverage obtained using the Q/QH_2 redox couple. Inset: E^{r}_{Q/QH_2} vs. pH plot for the redox couple (concentration $= 1 \times 10^{-3}$ M). The horizontal dashed lines indicate the potential selected for depositing Ag by using the Q/QH_2 redox couple (Reprinted with permission from Ref. [51])

potential $E^{r}_{Ag^+/Ag}$ and consequently Ag^+ reduction takes place in upd region. Figure 6.11b shows an adsorption isotherm obtained for Ag deposition on Au-NPs, as obtained from measurements from different authors, as reported in the work mentioned. The vertical dotted line indicates the potential fixed by the redox couple, at which the Au@Ag NP synthesis took place. For the sake of comparison, a voltammogram for Ag deposition on the surface of Au(111) can be observed in Fig. 6.11a, under similar conditions. We conclude that this work showed that the electric potential for metal deposition on free standing NPs suspended in solution can be continually tuned using reducing molecules (and their oxidized counterpart) with acid–base activity, in very much the same way that a potentiostat is used to

control the surface potential of an electrode. Thus, within this picture, the NP resembles a nanoelectrode that can be wired to a desired potential via a redox system.

We end the section stating that in analogy with the definition given for flat surfaces in section Chap. 3, metal deposition on NPs that are free in solution, can also be classified into:

- underpotential deposition (upd) for $E^{r}_{Q/QH_2} > E^{0}_{M/M^{z+}}$,
- overpotential deposition (opd) for $E^{r}_{Q/QH_2} < E^{0}_{M/M^{z+}}$.

This classification is relevant for the discussion given in the following section.

6.4 Thermodynamics of Underpotential Deposition at the Nanoscale

We will begin our analysis by considering a modelling similar to the one exposed in Sect. 6.2.3 of this chapter (see Fig. 6.3), with the difference that the analysis of thermodynamic stability will be made for a metal deposited on a NP, yielding a core@shell type NP. The model is shown in Fig. 6.12 and it consists of a typical

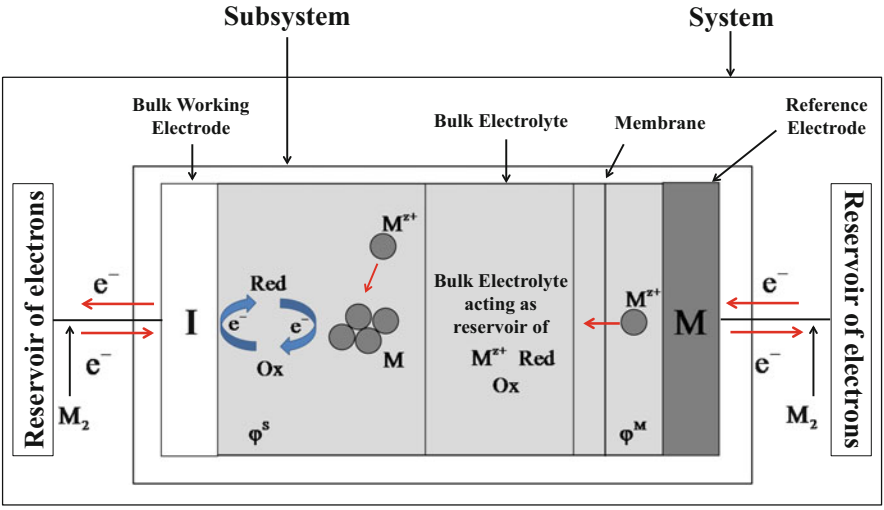

Fig. 6.12 Scheme of the electrochemical system used to analyze underpotential deposition on freestanding nanoparticles, where a redox system is used to set the potential applied to the metal nanoparticles. The broken line encloses the subsystem containing the electrodes, the nanoparticles, and the electrolyte. The broken line denotes a membrane that is permeable to all components of the system, with exception of the molecular species involved in the redox couple. The inner electrostatic potentials at both sides of the membrane are in principle different due to the presence of the redox system (Readapted with permission from Ref. [135])

electrochemical cell containing two infinitely large electrodes: the working electrode (W) and the reference electrode (R). The chemical species found in the electrolytic solution are metal ions to be deposited ($M^{z+}_{(aq)}$), the NPs made of a metal S, and the redox couple. The electrochemical cell is large enough so that the bulk properties of the electrolyte are not affected by the reactions on the surface of the NPs. We will denote this cell, that is, the electrolytic solution plus the two electrodes with the term "sub system" (see internal dotted line in Fig. 6.12). The later, together with the reservoirs will be called "system". While the subsystem is open, exchanging electrons and heat with the reservoirs; the complete system is isolated.

Let us consider for this system the free energy change due to the transfer of N_M atoms from the bulk electrode on the right to the surface of a NP on the left compartment.

First, N_M cations are generated at the electrode R and the electrons stemming from the metal oxidation go to electron reservoir, e^-_R:

$$M_{(bulk)} \rightarrow M^{z+}_{(aq)} + ze^-_R \tag{6.17}$$

These cations go through the membrane towards the left compartment:

$$M^{z+}_{(aq)\text{-right}} \rightarrow M^{z+}_{(aq)\text{-left}} \tag{6.18}$$

Since we assume that the membrane is permeable to the $M^{z+}_{(aq)}$ cations, the free energy change for this step is zero. Then, these cations are deposited on the surface of a NP made of p metallic atoms of S:

$$(N_M)M^{z+}_{(aq)} + zN_M e^-_{RC} + S_p \rightarrow S_p @ M_{N_M} \tag{6.19}$$

The electrons, e^-_{RC}, required for their reduction are provided from the simultaneous oxidation of the redox couple:

$$\left(\frac{zN_M}{n}\right)Red^u \rightarrow \left(\frac{zN_M}{n}\right)Ox^{u+n} + zN_M e^-_{RC} \tag{6.20}$$

Then, an electron exchange is allowed to take place on the surface of the I electrode (inert surface), returning the redox system to its reduced original state:

$$\left(\frac{zN_M}{n}\right)Ox^{u+n} + zN_M e^-_W \rightarrow \left(\frac{zN_M}{n}\right)Red^u \tag{6.21}$$

The electrons, e^-_W, required for this process are provided by the electron reservoir on the left. As result of this process, M deposition on the surface of the S-NP occurs. The electrochemical global reaction that takes place is:

$$N_{\mathrm{M}}\mathrm{M} + \mathrm{S_p} + (zN_{\mathrm{M}})\mathrm{e}_{\mathrm{W}}^{-} \rightarrow \mathrm{S_p}\,@\,\mathrm{Me}_{\mathrm{N_M}} + (zN_{\mathrm{M}})\mathrm{e}_{\mathrm{R}}^{-} \tag{6.22}$$

The related free energy of this reaction may be obtained using the free energy differences of products and reactants:

$$\Delta\widetilde{G} = \left[G^{\mathrm{Sp}}@\,\mathrm{M}_{\mathrm{N_M}} - G^{\mathrm{Sp}} - N_{\mathrm{M}}\mu_{\mathrm{M}}^{\mathrm{bulk}}\right] + zN_{\mathrm{M}}\left[\widetilde{\mu}_{\mathrm{e}}^{\mathrm{R}} - \widetilde{\mu}_{\mathrm{e}}^{\mathrm{W}}\right] \tag{6.23}$$

As shown above, when electronic equilibrium establishes at the left compartment, the electrochemical potentials of electrons at the NP, the redox system and the I electrode are equal. Thus, electrons from the reservoir on the left may reach the surface of the NP without the need of an electrical work.

In Sect. 3.1 of this book, it has been stated that the difference of the electrochemical potentials of electron corresponds to $\left(\widetilde{\mu}_{\mathrm{e}}^{\mathrm{R}} - \widetilde{\mu}_{\mathrm{e}}^{\mathrm{W}}\right) = ze_0\eta$, so that the previous Eq. (6.23) reduces to:

$$\Delta\widetilde{G} = \left[G^{\mathrm{Sp}}@\,\mathrm{M}_{\mathrm{N_M}} - G^{\mathrm{Sp}} - N_{\mathrm{M}}\mu_{\mathrm{M}}^{\mathrm{bulk}}\right] + ze_0N_{\mathrm{M}}\eta \tag{6.24}$$

Equation (6.24) looks very much like Eq. (3.71) of Chap. 3 for flat surface. We write, "looks very much like" because the contributions in Eq. (6.24) involve a number of subtleties not present in the case of upd on flat surfaces. The first is that the presence of the redox couple generates a difference between the inner potentials of the solution in the left and right compartments, say $\Delta\varphi$. Since the membrane separating the compartments of the cell has been assumed to be permeable to the $\mathrm{M}_{(\mathrm{aq})}^{z+}$ cations, the electrochemical potential in both compartments is the same. Thus, the activities of the cations must be different. Alternatively, if the membrane had been impermeable to the $a_{\mathrm{M}_{(\mathrm{aq})}^{z+}}$ cations and the same activity had been introduced in both compartments, a extra term $(-ze_0N_{\mathrm{M}}\Delta\varphi)$ would appear in Eq. (6.24).

The other difference between flat and curved surfaces concerning the free energy of formation of structures, is that ΔG in Eq. (3.71) involves an infinitely large surface, while in Eq. (6.24) the term in brackets corresponds to a finite system. Even more, since the present system is of nanoscopic size, the correct formalism to deal with it is nanothermodyanics, as established by Hill [35, 36]. To state these differences shortly, we can say that in the flat surface formulation ΔG is extensive with respect to the number of adatoms, in the sense that if we multiply the number of adatoms by a constant all the properties of the system will be scaled accordingly. In Eq. (6.24), this is not the case. This can be better understood if we consider the effects of the curvature. As the NP becomes of a smaller size, curvature effects become more important and in general, this fact gradually weakens the metallic bound. Thus, the properties of this type of systems are not extensive.

Figure 6.13 shows the qualitative behavior of $\Delta\widetilde{G}$ as a function of the number of M atoms, N_{M} deposited on a NP for systems presenting (a) opd and (b) upd. In the case of opd, Fig. 6.13a, the behavior of $\Delta\widetilde{G}$ looks very much like that usually found in the analysis of classical models of nucleation and growth, see discussion in

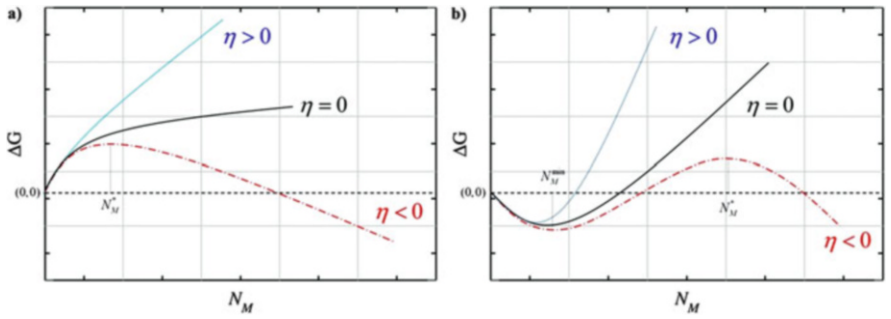

Fig. 6.13 Qualitative scheme of the excess Gibbs energy $\Delta\widetilde{G}$ as a function of the number of atoms N_M for the electrochemical formation of a core@shell nanostructure. (**a**) Corresponds to a situation where the interaction of the deposited atoms with the substrate, is weaker than the interaction with each other (opd). (**b**) Opposite case of (**a**), (upd) (Reprinted with permission from Ref. [136])

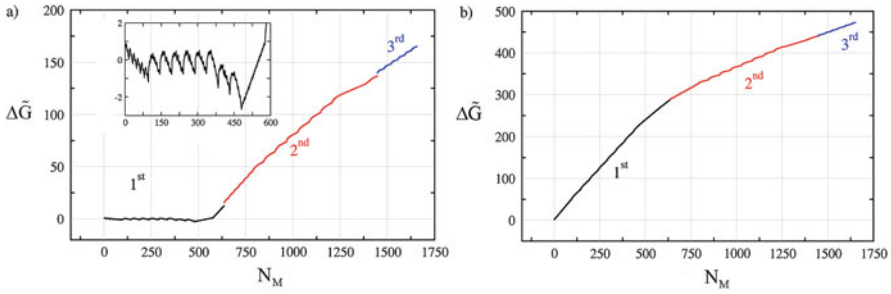

Fig. 6.14 Energy excess as discussed below Eq. (6.24) for the deposition of (**a**) Ag atoms and (**b**) Pd atoms on an Au NP made of 1289 atoms with octahedral structure. The different coloured lines denote in both cases the completion of a monolayer (Reprinted with permission from Ref. [26])

Sect. 6.2 (Fig. 6.3). The behavior for upd systems, shown qualitatively in Fig. 6.13b, is strikingly different. There, we find a minimum in the $\Delta\widetilde{G}$ vs. N_M curve for a number of adatoms that we denote with N_M^{min}. As discussed below, several minima may eventually occur. This minimum will eventually subsist at zero or slightly positive overpotentials, defining a global extremum. On the other hand, this minimum could also remain for slightly negative overpotentials, thus defining a local minimum or metastable state. This would imply the existence of core@shell nanostructures under overpotential conditions where bulk-growth should occur. The height of the free energy barrier, occurring at N_M^*, depends on overpotential, and so will the lifetime of the metastable state.

The qualitative picture presented in Fig. 6.13 has been verified by Grand Canonical Monte Carlo computer simulations [26]. Alternatively, Fig. 6.14 shows the behavior of $\Delta\widetilde{G}$ approximated from static energy calculations, as a function of the amount of metal atoms, which constitute the shell. The results shown are for the deposition of Ag atoms on an Au (1289) truncated octahedral NP and for the deposition of Pd atoms on an Au (1289) NP. We note that the general behavior is

similar to Fig. 6.13. However, the discrete atomic nature and the packing of atoms in the NP produce deviations from the simplified behavior shown there. A magnification of Fig. 6.14a (see inset) shows a more complex sawtooth behavior, with 14 maxima, grouped into two families (6 + 8). These maxima correspond to a 2D nucleation and growth phenomenon located on each of the facets of the truncated octahedron. However, this saw motif should be wiped out by thermal effects at 300 K. While decoration of the NP is expected at zero overpotentials for the system Au(1289)@Ag (Fig. 6.14a), no spontaneous decoration is predicted for the system Au(1289)@Pd (see Fig. 6.14b).

Equation (6.24) can also be obtained from statistical mechanical considerations [26]. The partition function $\Upsilon(\mu_M, S_p, T)$ of the nanosystem shown in Fig. 6.12 is:

$$\Upsilon\left(\mu_M, S_p, T\right) = \sum_{N_M=0}^{\infty} Q\left(N_M, S_p, T\right)\exp[\beta N_M \mu_M] \tag{6.25}$$

where $Q(N_M, S_p, T)$ corresponds to the canonical partition function and $\beta = (k_B T)^{-1}$. Using Eq. (6.24), Eq. (6.25) can be rewritten in term of excess quantities:

$$\Upsilon\left(\mu_M, S_p, T\right) = A\sum_{N_M=0}^{\infty} \exp\left[-\beta\Delta G^{sub}\right]\exp[-zF\beta N_M \eta] \tag{6.26}$$

where $A = \exp\left[-\beta G^{S_p}\right]$. According to statistical mechanics, this equation contains all we need to calculate the thermodynamic properties of the NP system, since from it, all equilibrium properties may be calculated. However, there are at least two handicaps for such a calculation. One is the calculation of the free energy change ΔG^{sub} which in turn implies knowledge of the canonical partition function $Q(N_M, S_p, T)$. This calculation involves the sum over all energy states compatible with N_M, S_p and T. Even assuming a lattice model, and thus restricting the positions of the M and S atoms to a finite number of point in the configurational space, such a calculation appears as computationally extremely demanding due to the number of possible permutations. The other additional problem is the existence of infinite many terms in the sum of Eq. (6.26).

In Sect. 6.2.2, we presented the Hill-Chamberlin Model applied to understand supersaturated metastable states. It is possible to apply the same formalism to the case of under/over potential deposition. To show this, let us consider the probability of having N_M metallic atoms deposited on a NP made of S_p atoms at the overpotential η and temperature T:

$$p_{N_M}\left(\eta, S_p, T\right) = \frac{\exp\left[-\beta\Delta G^{sub} - zF\beta N_M \eta\right]}{\Upsilon\left(\mu_M, S_p, T\right)} \tag{6.27}$$

Since for given conditions the $\Upsilon(\mu_M, S_p, T)$ is a constant, we have that the product $p_{N_M}\left(\eta, S_p, T\right)\ \Upsilon(\mu_M, S_p, T)$ is monotonic with $p_{N_M}\left(\eta, S_p, T\right)$ and also its $(k_B T)^{th}$ power:

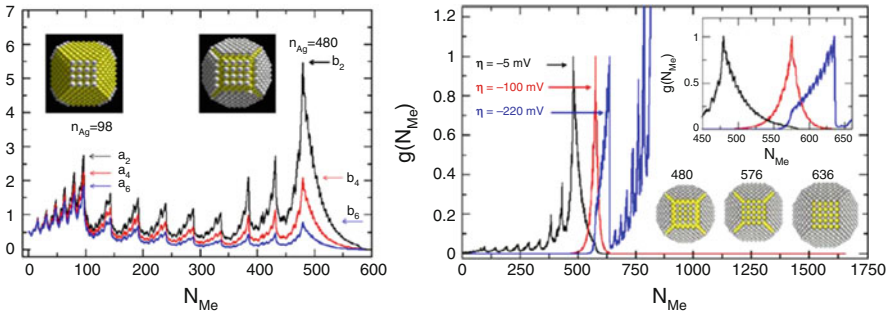

Fig. 6.15 Probability density of observing N_M Ag atoms deposited on a truncate octaedral Au (1289) core as a function of the number of atoms that conform the shell at different (**a**) underpotentials and (**b**) overpotentials (Reprinted with permission from Ref. [26])

$$f(N_M) = \left[p_{N_M}(\eta, S_p, T)\Upsilon(\mu_M, S_p, T)\right]^{k_B T} \tag{6.28}$$

thus, plot representation of $f(N_M)$, that can be calculated from Eq. (6.24), yields a straightforward visualization of minima and maxima in $p_{N_M}(\eta, S_p, T)$ without knowledge of $\Upsilon(\mu_M, S_p, T)$.

Figure 6.15a shows the $f(N_M)$ representation for the underpotential region ($\eta > 0$) for a NP of Au(1289) with truncated octahedral shape at 300 K, obtained for computer simulations [26]. We can note the convergence of the sum, for $N_M > 600$. For η close to the bulk deposition potential of M, $0 < \eta < 4$ mV, the system presents the highest probability at $N_M \approx 480$ (note $a_2 < b_2$ in Fig. 6.15a). In this region an ensemble of systems should be mainly composed of core–shell NPs with a coverage close to 75 %. At $\eta \approx 4$ mV the system has a2 ≈ b2 and therefore we would observe the coexistence of particles with two different coverages. At larger η, for example in the range of 4 mV $< \eta <$ 13 mV, the highest probable density is for a coverage close to 15 %, where $N_M \approx 98$. This value corresponds to the decoration of all {100} facets.

In the overpotential region, the sum (6.26) will diverge and some physical considerations must be made to get physical insight into the present problem in spite of this mathematical divergence. Figure 6.15b shows the normalized $f(N_M)$ (to its maximum value) for the same conditions as in Fig. 6.15a but for $\eta < 0$ (overpotential). The local maximum is shifted from $N_M \approx 480$ to $N_M \approx 636$ for -5 mV $< \eta < -220$ mV (See inset in Fig. 6.15b). Similarly to the observation within the HC model, as the overpotential becomes more negative (oversaturation), the mathematical divergence of the probability function is shifted towards lower N_M.

We must note that for the present system the core-shell structure is not completely formed at underpotentials, and due to border effects, it requires large negative overpotentials to occur. However, large negative overpotentials will make the monolayer eventually unstable and a multilayer will appear.

6.5 Atomistic Model for Underpotential Deposition on Nanoparticles

In order to make a qualitative analysis, a simplified model can be set up that allows describing ΔG^{sub} in terms of the geometry of the NP. Figure 6.16 shows a scheme of the simplified model we address here. We define three regions in the system: an inner part (inner), an intermediate part (intermediate), and an external part (monolayer). The former two belong to the pre-existing seed and they build the core of a core@shell structure in the case of heteroatomic growth.

We will characterize the energy of the inner atoms by the chemical potential of the bulk S atoms, $\mu_{\text{S}}^{\text{bulk}}$ and define two types of atoms in the intermediate region: those located on the facets, characterized by the free energy $g_{\text{S}}^{\text{facet}}$, and those located at border sites, with the free energy $g_{\text{S}}^{\text{border}}$. In the case of the monolayer, we also differentiate between facet and border adatoms, with their free energies given by $g_{\text{S/M}}^{\text{facet}}$ and $g_{\text{S/M}}^{\text{border}}$ respectively, see Fig. 6.16.

According to the model mentioned before, the Gibbs free energy of the core (initial state) may be approximated as:

$$G^{\text{S}_{\text{p}}} = N_{\text{S}}^{\text{core}} \mu_{\text{S}}^{\text{bulk}} + N_{\text{S}}^{\text{facet}} g_{\text{S}}^{\text{facet},0} + N_{\text{S}}^{\text{border}} g_{\text{S}}^{\text{border},0} \tag{6.29}$$

As we will analyze later, the second term of the right side of the equality (6.29) may be interpreted as the "surface" effects while the third term can be interpreted as "curvature" effects. On the other hand, the Gibbs free energy of the core@shell NP may be estimated as:

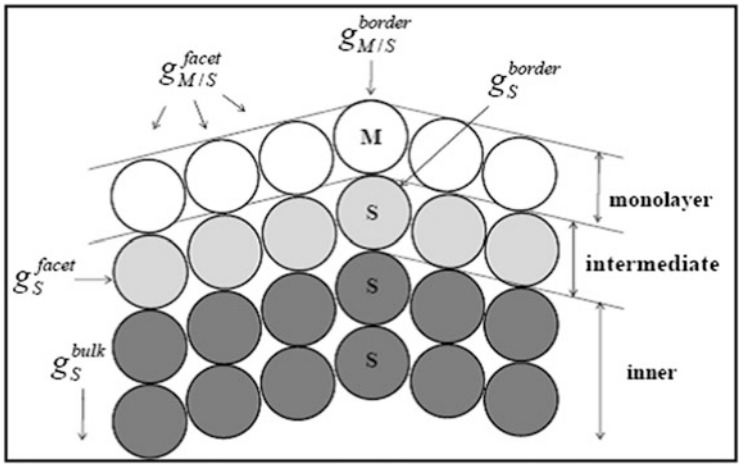

Fig. 6.16 Schematic representation of the simplified model used to analyze upd on NPs, described in terms of five different atom types

$$G^{S_p@M_{N_M}} = N_S^{core}\mu_S^{bulk} + N_S^{facet}g_S^{facet,0} + N_S^{border}g_S^{border,0} + N_{S/M}^{facet}g_{S/M}^{facet} + N_{S/M}^{border}g_{S/M}^{border} \quad (6.30)$$

We should notice that $g_S^{facet,0} \neq g_S^{facet}$ and that $g_S^{border,0} \neq g_S^{border}$ given that the presence of the shell modifies the configuration (and the energy) of the core surface layer. The difference of formation energy may be estimated by subtracting Eq. (6.30) from Eq. (6.29), so that:

$$G^{S_p@M_{N_M}} - G^{S_p} = N_S^{facet}\left(g_S^{facet} - g_S^{facet,0}\right) + N_S^{border}\left(g_S^{border} - g_S^{border,0}\right) + N_{S/M}^{facet}g_{S/M}^{facet} + N_{S/M}^{border}g_{S/M}^{border} \quad (6.31)$$

Equation (6.31) indicates that the free energy change $G^{S_p@M_{N_M}} - G^{S_p}$ only depends on the energetic of the two more external layers. ΔG^{sub} can be estimated as:

$$\Delta G^{sub} = N_S^{facet}\left(g_S^{facet} - g_S^{facet,0}\right) + N_S^{border}\left(g_S^{border} - g_S^{border,0}\right) + N_{S/M}^{facet}\left(g_{S/M}^{facet} - \mu_M^{bulk}\right) + N_{S/M}^{border}\left(g_{S/M}^{border} - \mu_M^{bulk}\right) \quad (6.32)$$

It can be noticed that N_S^{facet} and $N_{S/M}^{facet}$ are linearly related, such as $N_S^{facet} = \kappa N_{S/M}^{facet}$, where κ is a geometrical coefficient (generally $\kappa > 1$). The same occurs for N_S^{border} and $N_{S/M}^{border}$. We can rewrite the previous equation as:

$$\Delta G^{sub} = N_{S/M}^{facet}\left(g_{S/M}^{facet,eff} - \mu_M^{bulk}\right) + N_{S/M}^{border}\left(g_{S/M}^{border,eff} - \mu_M^{bulk}\right) \quad (6.33)$$

Then, $\Delta\widetilde{G}$ may be estimated from:

$$\Delta\widetilde{G} = N_{S/M}^{facet}\left(g_{S/M}^{facet,eff} - \mu_M^{bulk} + ze_0\eta\right) + N_{S/M}^{border}\left(g_{S/M}^{border,eff} - \mu_M^{bulk} + ze_0\eta\right) \quad (6.34)$$

The present model implies that the excess of energy has at least two components: one related to the facets and other related to the borders. If $N_{S/M}^{border} << N_{S/M}^{facet}$ as it is the case for relatively large NPs, $\Delta\widetilde{G}$ is reduced to the behavior of an infinitely flat surface.

The generalization of model for NPs formed by different types of facets and borders is straightforward:

$$\Delta\widetilde{G} = \sum_{i}^{\text{sites}} N_{\text{S/M}}^{\text{i}} \left(g_{\text{S/M}}^{\text{i,eff}} - \mu_{\text{M}}^{\text{bulk}} + ze_0\eta \right) \tag{6.35}$$

6.6 Strengthening and Weakening of Underpotential Deposition at the Nanoscale. Underpotential Deposition-Overpotential Deposition Transition

To analyze a little more in detail how curvature effects play a role in favor or against upd, we can consider a relationship between $N_{\text{S/M}}^{\text{border}}$ and $N_{\text{S/M}}^{\text{facet}}$, within a given family of NPs, that is, with a particular geometry. In a general way, we can define $N_{\text{S/M}}^{\text{border}} = \delta \left(N_{\text{S/M}}^{\text{facet}} \right)^{1/2}$ where $\delta > 0$ is a geometrical factor that depends on the shape of the NP. In this way, the number of variables in Eq. (6.34) can be reduced. In this context, we can find from the later equation that [52]:

$$\Delta\widetilde{G} = 0 \quad \Rightarrow \quad N_{\text{S/M}}^{\text{facet},*} = \left[\delta \frac{\left(g_{\text{S/M}}^{\text{border,eff}} - \mu_{\text{M}}^{\text{bulk}} + ze_0\eta \right)}{\left(g_{\text{S/M}}^{\text{facet,eff}} - \mu_{\text{M}}^{\text{bulk}} + ze_0\eta \right)} \right]^2 \tag{6.36}$$

$N_{\text{S/M}}^{\text{facet},*}$ must be interpreted as a threshold value that must be overcome for a thermodynamically spontaneous deposition, with $\Delta\widetilde{G} < 0$. The number $N_{\text{S/M}}^{\text{facet},*}$ is straightforwardly related to the total number of atoms in the shell N_{M}, since $N_{\text{M}} = N_{\text{S/M}}^{\text{border}} + N_{\text{S/M}}^{\text{facet}}$.

The reason for the system to present a $\Delta\widetilde{G} < 0$ lays on the strong interaction between adsorbate and substrate in the facets. In the case of infinite planar surfaces, this is the interaction responsible for upd. If metal atoms deposited on a facet of S are more stable than in the bulk state, $g_{\text{S/M}}^{\text{facet,eff}}$ will be more negative than $\mu_{\text{M}}^{\text{bulk}}$ and we will have the inequality $\left(g_{\text{S/M}}^{\text{facet,eff}} - \mu_{\text{M}}^{\text{bulk}} \right) < 0$. Let us analyze the consequence of this condition in Eq. (6.34), for $\eta = 0$, which becomes equal to Eq. (6.33). Since the second term in Eq. (6.33) is usually positive, the condition $\Delta\widetilde{G} = 0$ will be fulfilled at some $N_{\text{S/M}}^{\text{facet},*}$. Thus, the adsorbate atoms will subsist on the surface of S at more positive potentials than the Nernst reversible potential for bulk M deposition. This reminds us the occurrence of the upd phenomenon on flat metal surfaces. The reverse situation will take place when $\left(g_{\text{S/M}}^{\text{facet,eff}} - \mu_{\text{M}}^{\text{bulk}} \right) > 0$, since ΔG^{sub} in Eq. (6.33) will be always positive. The latter is clearly an unsuitable condition for size and shape control of nanosystems since when $\eta < 0$, the bulk deposit can be formed so that the application of an overpotential allowing the deposition on S should inevitably drive it to M-bulk growth, at least from a thermodynamic viewpoint. In the model described in Fig. 6.16 and Eqs. (6.28), (6.29), (6.30),

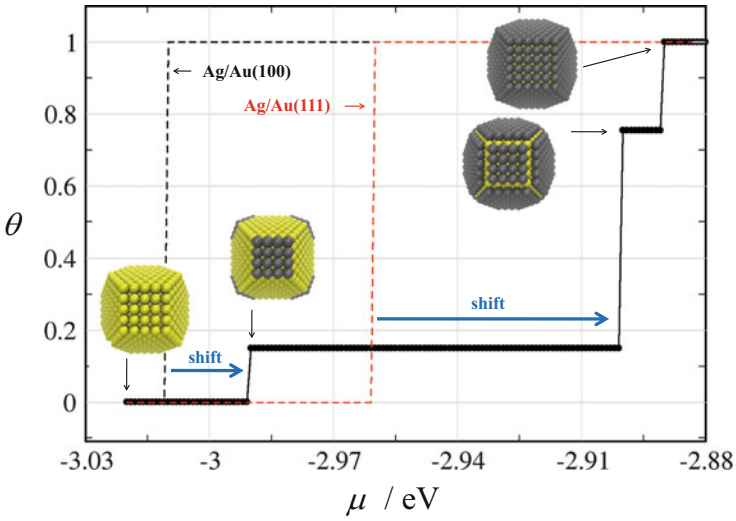

Fig. 6.17 Adsorption isotherms for Ag deposition on a Au truncated octahedral nanoparticle made of 1289 atoms. For comparison, the isotherms corresponding to Ag deposition on Au(100) (*black dashes*) and Au(111) (*red dashes*) are shown

(6.31), (6.32), (6.33), (6.34), and (6.35), $g_{S/M}^{facet}$ and $g_{S/M}^{border,eff}$ have been assumed to be constant. In the real case, these quantities are a function of NP size.

Figure 6.17 shows adsorption isotherms for Ag adsorption on a Au NP of octahedral shape, as well as on planar Au(111) and Au(100) surfaces. These were obtained from lattice Grand Canonical Monte Carlo simulations using embedded atom potentials. It is illustrative to compare the potentials at which the {111} and {100} facets are filled, in comparison with the decoration of the infinite surfaces. It is found that in the case of the NP, curvature plays a destabilizing role concerning upd. It can be noted that while upd on (111) and (100) faces occur at $\mu_{Au(111)/Ag}^{bulk} \approx -2.968$ eV and $\mu_{Au(100)/Ag}^{bulk} \approx -3.018$ eV, the related processes on the facets of the NP take place at $\mu_{Au\{111\}/Ag}^{NP} \approx -2.907$ eV and $\mu_{Au\{100\}/Ag}^{NP} \approx -2.990$ eV. These values correspond to shifts in the deposition chemical potentials of $\Delta\mu_{Au\{111\}/Ag}^{NP} \approx 61$ mV of $\Delta\mu_{Au\{100\}/Ag}^{NP} \approx 28$ mV for the {111} and {100} facets respectively. Thus, these simulations clearly show the existence of a positive shift of metal deposition towards larger chemical potentials for nanoparticles, thus weakening upd. We remind that more positive chemical potentials correspond to more negative electrode potentials in the electrochemical scale.

Going back to Eq. (6.36) for NPs, we find that the stronger the border effects, given by the $\left(g_{S/M}^{border,eff} - \mu_M^{bulk}\right)$ term, the larger the NP size at which the upd-opd transition occurs will be. On the opposite, systems with large upd shifts in flat surfaces, involving a large $\left(g_{S/M}^{faceta,eff} - \mu_M^{bulk}\right)$ contribution, will present the upd-opd transition at smaller NP sizes. According to computer simulations, upd has been predicted to disappear for small particles sizes in the Au(core)/Ag(shell)

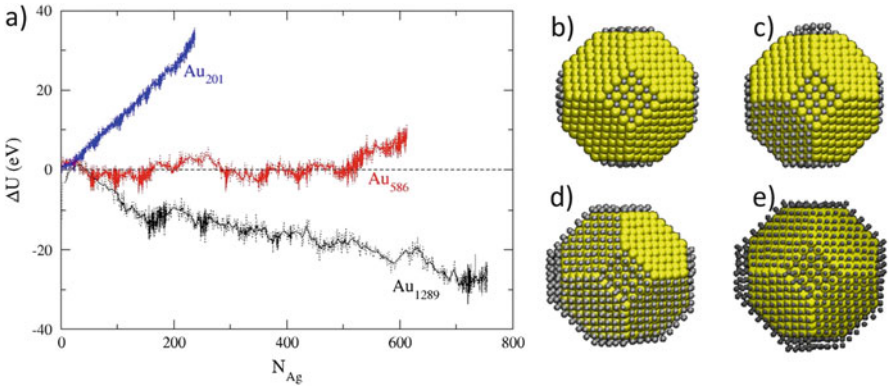

Fig. 6.18 (**a**) Excess energy as a function of the number of deposited Ag atoms for Au nanoparticles of different sizes at $\eta = 0$. Representative atomic configurations taken for Au (1289) at (**b**) $\eta = -220$ mV, (**c**) $\eta = -40$ mV, (**d**) $\eta = -20$ mV, and (**e**) $\eta = 0$ (Reprinted with permission from Ref. [136])

[25, 26, 136, 137] and Au(core)/Pd(shell) systems [52]. In the experimental field, there is evidence that upd may disappear for Pb and Cd deposition on Ag NPs [138, 139, 140]. Figure 6.18 shows Off-Lattice Gran Canonical Monte Carlo (GCMC) simulations for the system Au(core)@Ag(shell), where it comes out that the upd phenomenon disappears for core sizes smaller than 512 atoms. Representative snapshots of GCMC simulations, corresponding to different overpotentials, are presented on the right of Fig. 6.18b–e, where selective decoration of some facets of the NP becomes evident.

In the case of systems with relatively strong substrate-adsorbate interactions, it is possible to obtain an adsorbate bilayer at underpotentials, as was discussed in Chaps. 2 and 3. Following the preceding discussion, bilayer upd may also be weakened (strengthened) by the occurrence of positive (negative) curvatures. According to theoretical predictions, this should be the case of the system Pd@Au(bilayer). For this system, we have calculated the excess potential energy using Pd-seed NPs of icosaedral structure with different sizes, on which different numbers of atomic layers of Au-adsorbate were located. These excesses are shown in Fig. 6.19. When analyzing Fig. 6.20, it must be taken into account that the curves connect systems with the same number of layers. For example, the black curve connects Pd(13)@Au(42), Pd(55)@Au(92), Pd(147)@Au(162), Pd(309)@Au (252), Pd(561)@Au(362) and Pd(923)@Au(492), that is, increasing Pd core sizes, always covered by a Au monolayer. As can be observed, the free energy excess for small NPs is positive. However, the excess of free energy for monolayer formation turns negative for Pd(309)@ Au(252) and remains negative for larger cores, indicating that upd could be possible for larger NPs. It is also remarkable that the curve for the formation of the bilayer presents a maximum, indicating that for larger NP sizes bilayer formation could be spontaneous at $\eta = 0$.

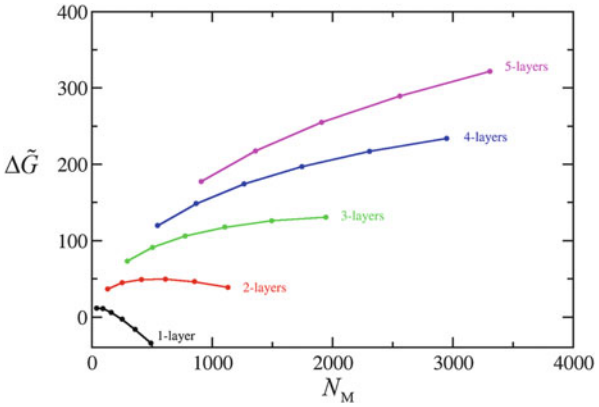

Fig. 6.19 Excess of binding free energy for the formation of a Pd(core)@Au(shell) nanoparticle as a function of the number of atoms forming the shell. Each curve corresponds to a given number of adlayers deposited on different core sizes (Reprinted with permission from Ref. [141])

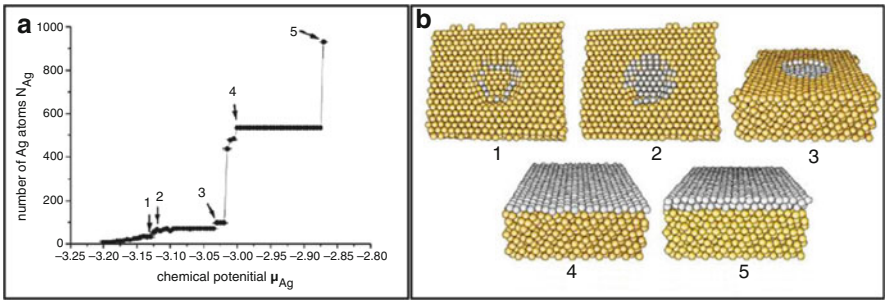

Fig. 6.20 Number of deposited Ag atoms as a function of the chemical potential for decoration of a nanocavity on a Au(111) surface. (**b**) Snapshots of the simulation showing the different stages of nanohole decoration, corresponding to the numbers of part (**a**). The chemical potentials were $\mu_{Ag} = -3.155$ eV, $\mu_{Ag} = -3.12$ eV, $\mu_{Ag} = -3.03$ eV, and $\mu_{Ag} = -3.00$ eV (Reprinted with permission from Ref. [53])

Going back to the nanohollow case, computer simulations of this phenomenon were undertaken by Luque et al. [53] using the Off-Lattice GCMC methodology. These studies showed that depending on the interaction between the adsorbate and the substrate as compared with the adsorbate–adsorbate interactions, the deposit may grow defining a cluster over the surface level, like Au(111)/Cu or heal the damage on the surface with the subsequent formation of a monolayer, like Au(111)/Ag. In the former case, Cu deposition remains confined to the defects generated on the surface, since the formation of clusters on the Au(111) is disfavoured. On the contrary, Ag deposition on the flat Au(111) surface occurs after the filling of the nanocavity.

Figure 6.20 shows the results from Off-Lattice GCMC atomistic simulations for the decoration of nanocavities on Au(111) with Ag atoms. The decoration of the

nanocavity starts at $\mu_{Ag} = -3.155\,eV$ at its bottom, being the first Ag atoms deposited on the border sites. The basis of the nanocavity becomes completely covered at $\mu_{Ag} = -3.12\,eV$ and its filling occurs at $\mu_{Ag} = -3.03\,eV$. All these processes take place at chemical potentials more negative than that corresponding to the bulk Ag metal, $\mu_{Ag} = -3.00\,eV$. These atomistic simulations showed for the first time that negative curvatures allow metal deposition at more negative chemical potentials (more positive electrode potentials en the electrochemical scale) than those corresponding to upd on planar surfaces with the same crystal orientation.

6.7 Experimental Research

Although a bimetallic nanocrystal consists of only two elements, it may exist in many different structures depending on the spatial distributions of these two elements. We will describe some techniques of electrochemical origin that allow the manipulation of this degree of freedom, as follows:

6.7.1 Seed-Mediated Growth

The growth of NPs or nanorods (NRs) mediated by seeds has demonstrated to be an easy and versatile route for metallic nanocrystal formation with well-defined size and shape [16, 54–57]. Originally, Zsigmondy called this technique "nuclear method" [58] and its origin dates from the beginning of last century. In 1920, Svedberg stated that any reducing agent (known at that time) could produce Au-NPs from $HAuCl_4$ [59]. The technique is very versatile and can be applied in aqueous systems as well as in organic systems [60, 70] at different temperatures and for a large number of systems that include Au, Ag, Pd and Pt [30, 48, 61–71]. The first step consists in the production of clusters and/or NPs which may be used as growth seeds. Generally, this process is called "first nucleation". Metallic salts may be reduced at room temperature with a strong reducing agent (for example, borohydride). It is necessary to overcome the large barrier of homogenous nucleation for the formation of a new phase. In a second stage, this preformed seeds are put into a solution to serve as preferential sites for a new process of nucleation and growth. This second step is called "growth stage". The growth of a second metal can be involved in this second stage, or not. In Sect. 6.2.2 we discussed these topics and we presented the LaMer model to understand the behavior of the phases in this stage.

The driving force for NP growth is the difference between the redox potentials (ΔE) of the two reactions (metallic reduction and oxidation of the reducing agent). A larger ΔE means a more spontaneous reaction. Reagent concentration,

temperature, and pH influence the growth kinetics as well as the size, shape and structure of the final NPs. For example, a strong reducing agent such as $NaBH_4$ or phosphorus can be used for the production of small size Au NPs, while ascorbic acid –a weak reducing agent – produces larger NPs. NP aggregation can be avoided through a strong shaking or by adding stabilizing agents.

Homogeneous nucleation and growth generally produces irregularly shaped particles and a wide size distribution. The activation energy for the process of heterogeneous nucleation is significantly lower than the activation energy for the process of homogeneous nucleation. As a result, heterogeneous nucleation is thermodynamically favored with respect to homogeneous nucleation. While homogeneous nucleation and growth can be described in terms of a curve like that shown in Fig. 6.13a, its heterogeneous counterpart can be represented by Fig. 6.13a or Fig. 6.13b, depending on the effective interactions between the elements that constitute the core and the shell. In practice, seed-mediated growth takes place at a relatively slow rate in soft conditions, such as those provided by a weak reducing agent and/or low temperatures. The reduction on the surface of the seed can be viewed as an autocatalytic process. As the NP acquires a larger size, the nucleation barrier becomes smaller.

In general, metals tend to nucleate and grow in thermodynamically stable nanoparticles, which exhibit a compact shape. These NPs expose facets of low energy in order to minimize the total energy of the surface. Highly anisotropic shapes are not favorable from the thermodynamic point of view, but can be obtained by inserting agents that can alter the surface energies of the different crystallographic faces [71]. Carbó-Argibay et al. [61] analyzed in detail the growth of Au nanorods (NRs) using well-characterized Au-NPs as growth seeds. Initially, see Fig. 6.21a, the NRs present eight {110} and {100} facets, alternated in their lateral parts. Their tips consist of {001}, {110} and {111} facets. The first step in the

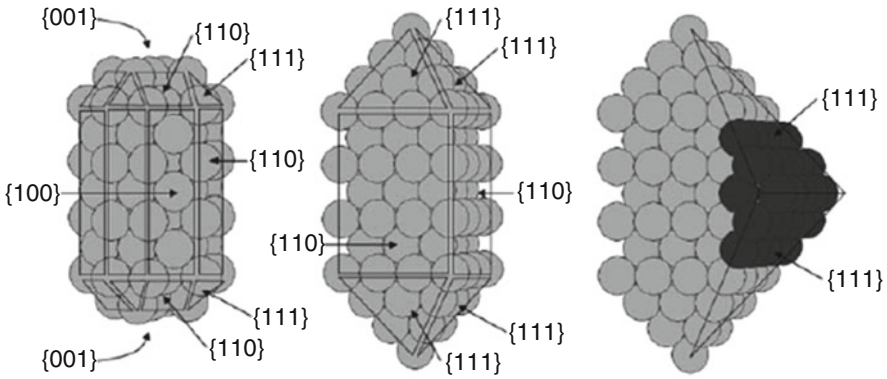

Fig. 6.21 Structural model of Au nanorod growth. *Left*: Original nanorod with octagonal cross-section and {100}, {110}, {111} facets. *Center*: Rod with sharp tips, square cross-section, {110} and {111} facets. *Right*: Growth of a sharpened rod into an octahedral particle by deposition of Au atoms (*dark spheres*) along the {110} facets (Reprinted with permission from Ref. [61])

growth consists in the preferential deposition of Au atoms on the 4 {100}-type facets from the lateral part and on the 2 {100}-type facets at the tips (see Fig. 6.21b). As a result, 4 lateral {110} facets were obtained, as well as sharp tips made from 4 {111} facets (Fig. 6.21b). The second growth stage consisted in a morphological transition to become an octahedron. This is produced by means of a delicate balance between the growth rates on facets {110} and {111}. Fig. 6.21c shows schematically the growth on {110}-type facets, forcing facets {111} to grow until they join in the final octahedral structure.

The mechanism described in Fig. 6.21, is based on the preferential growth of certain crystal facets. It could be formally correlated with the sequence of surface energies in the following order: $\{100\} > \{110\} > \{111\}$. This does not agree with the sequence of surface energies of Au, which follows the order: $(110) > (100) > (111)$. However, as these authors noted in Reference [61], the effective values of surface energies can be affected by the adsorption of chemical species such as ions and molecules in a significant way and thus, they can be assumed to be responsible for such changes and could explain such a tendency. Although there is no concrete evidence to support these assumptions, these results show that the crystallographic structure of the seeds, together with the chemical nature of the bath where they grow, play a key role in the determination of the NPs final structure and shape. Thus, these results present a strong indication that surfactant ions and molecules can affect the growth kinetics and can help to control the final shape of the NPs. For example, citrate binds strongly to Pd {111}-type facets, leading the synthesis towards octahedra and icosahedra formation [72]. In contrast, polyvinylpyrrolidone is a protecting agent, which binds stronger to Pd {100}-type facets, favoring the formation of truncated cubes [73, 74]. Besides, bromide ions promote Pd-NP formation exposing {100} facets [75].

A versatile approximation to the formation of bimetallic NPs core@alloy type is called co-reduction mediated by seeds [76–78]. In this technique, two metallic precursors are simultaneously reduced on a NP used as growth seed. This technique allows control of the NP morphology, obtaining branched NPs commonly called nanodentrites. DeSantis et al. [76] made a systematic study on the influence of synthesis conditions on the morphology of nanodendrites. These authors analyzed the role of the concentration of precursors (ratio Au/Pd), reaction pH, and concentration of NP protecting agent. For example, Fig. 6.22 shows the structural variation of Au/Pd NPs at different *p*H values for otherwise the same reaction conditions. The pH was adjusted by adding different amounts of HCl to the system (from A up to F corresponds to 2 mL of 0.0, 12.5, 25.0, 37.5, 50.0, and 62.5 mM HCl, respectively). Pd became dispersed all over the surface of the octopods and became localized along the tips of the branched nanostructures, with Au predominating in the interior of the particles (Fig. 6.22 4A, 4B). We note that Pd-rich regions appear lighter in TEM and STEM images, as $Z_{Au} > Z_{Pd}$. With decreasing *p*H, the SEM images reveal regions of negative curvature associated with the absence of {100} facets of what would otherwise be cuboctahedral particles (Fig. 6.22 4C–4E). Finally, a perfect octahedral NP was obtained at a relatively low pH (Fig. 6.22 4F). At a larger content of HCl (lower pH) the inner part of the NPs becomes more abundant in Au and

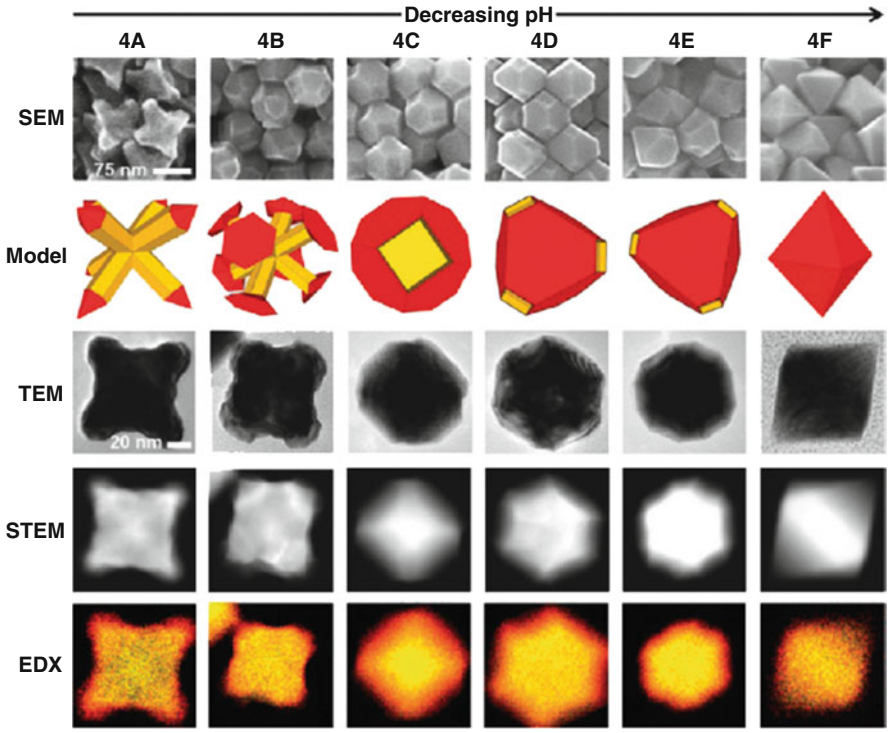

Fig. 6.22 From *top* to *bottom*, AuPd nanocrystals characterized by higher magnification SEM as well as 3D models (yellow represents Au-rich and *red* represents Pd-rich regions), TEM, STEM, and STEM-EDX mapping (*yellow* indicates Au and *red* indicates Pd). Note: all SEM images are at the same magnification. Similarly, TEM, STEM, and STEM-EDX mapping are at the same magnification (Reprinted with permission from Ref. [76])

show cuboctahedral or octahedral structures. These are thermodynamically favored structures. In opposite conditions, at high pHs, the amino acid reducing capacity is larger; consequently, the reduction velocity is faster and the system has not enough time to re-adapt, thus obtaining structures very different from the ones predicted by thermodynamics (kinetic control). Another way to control morphological changes is the formation of complexes with CTAB by etched Au. It is known that the Au oxidation rate under these conditions depends on pH, so that the regions with larger curvature are more prone to oxidation [79].

As a corollary to this section and the following, we can state that all the information gained through research about the effect of solution composition (ions, molecular adsorbates) on the stability of upd deposits on single crystal surfaces is worth being analyzed with the aim of their application to the synthesis of NPs. Alternatively, many of the questions arising in the synthesis of nanoparticles may probably be answered by means of electrochemical studies of metal upd (and the related galvanic replacement technique) on single crystal surfaces.

6.7.2 *Shape Control of Nanoparticles Synthesis by Underpotential Deposition*

Liu and Guyot-Sionnest [80] proposed, in 2005, an explanation for the role of Ag ions in the directed growth of Au NPs. They suggested that upd of metallic silver occurs at different extents on the different crystal facets of Au NPs, leading to symmetry breaking and rod formation. It is known that upd of Ag is stronger on more open surfaces, involving the sequence stability $\{111\} < \{100\} < \{110\}$. In fact, electrochemical measurements yielded underpotential shifts of 0.24 and 0.07 V for Ag upd on Au{100} and Au{111} surfaces, respectively [81, 82]. The same trend has been found in theoretical calculations, predicting that the upd shift should be 0.14 V for Ag on Au(100) and 0.10 V for Ag on Au(111) [83]. As a consequence of this, an appropriate tuning of the deposition potential would allow decorating selectively facets (see Figs. 6.17 and 6.18). Similarly, a silver monolayer on the Au{110} facet acts as a strong binding agent, inhibiting further growth, so that other low index faces grow faster and become dominant in the final structures. The {100} and {111} facets are only partially covered by silver or remain adsorbate free, and therefore grow faster than {110}. This leads to a one-dimensional growth along one direction. The growth rate ratio between {100} and {110} facets is adjustable by varying the Ag^+ concentration. Then, upd provides a general mechanism to control shape evolution in metallic nanostructures [84].

Seo et al. [85, 86] determined the major influencing factor for shape conversion of cuboctahedral NPs. Cuboctahedral NPs are built from {100} and {110} facets, as shown in Fig. 6.23a (middle picture) and Fig. 6.23c. Ag^0 reduced from Ag^+ was preferentially deposited onto the {100} facet to form silver layers, which suppressed epitaxial overgrowth of the gold layers during the reaction. The {111} facets grew producing changes in the NP morphology. This change transformed the NPs from octahedral shapes to cuboctahedral and then to cubic shapes (Fig. 6.23a, d). In the absence of silver ions, the addition of Au^{3+} precursor enhances {100} growth to increase the surface fraction of {111} facets. That process makes cuboctahedral NPs to become octahedral ones, where only {111} facets are present (Fig. 6.23a, b). This procedure was also applied for redirecting and controlling Pt NPs growth [87].

Mirkin and coworkers [88] have also shown that a fine control of NP shape is possible using Ag upd to direct the growth of different Au-NPs morphologies: for example, octahedrons with {111} facets, rhombic dodecahedrons with {110} facets, truncated ditetragonal prisms with {310} facets, and concave cubes with {720} facets. In a later work, Mirkin and coworkers [89] analysed in detail the effect of including other additives like chloride, bromide and iodide on NP growth under Ag-upd control. These authors showed how different sets of NP shapes can be obtained via kinetic control, surface passivation, or a combination of both. A number of important findings emerged from this work, some of them are:

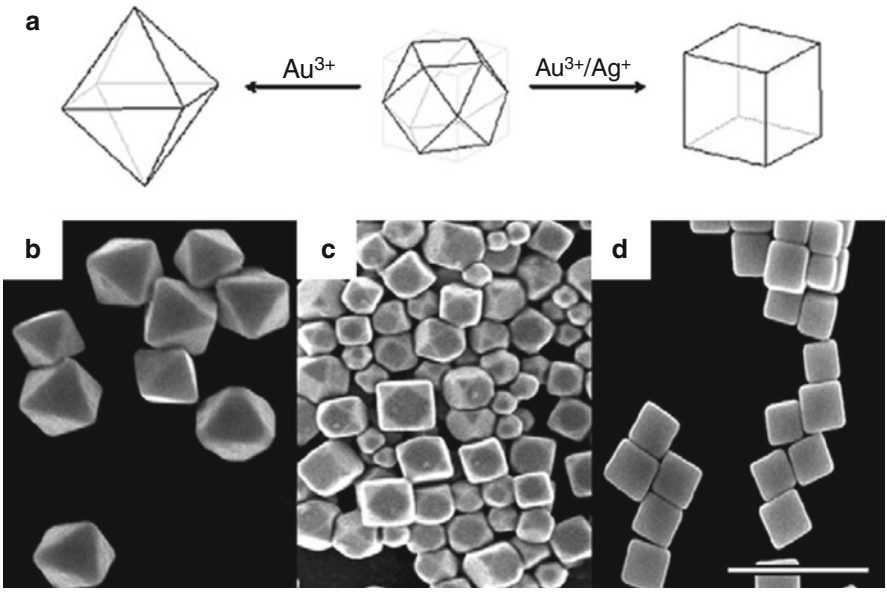

Fig. 6.23 (**a**) Shape evolution of cuboctahedral seeds by changing the growth solutions. SEM images of (**b**) large octahedra grown by addition of the gold precursor, (**c**) cuboctahedral seeds, and (**d**) cubes grown by addition of Ag^+ and the gold precursor. The bar represents 500 nm (Reprinted with permission from Ref. [86])

(a) In the absence of bigger halides (bromide and iodide), increasing concentrations of silver ions stabilize particles with a larger number of exposed surface atoms per unit surface area, enabling the formation of high-index nanostructures.
(b) In the presence of silver ions as a shape-directing additive, the addition of a large amount of the bigger halides (bromide and iodide) greatly decreases the stability of the Ag upd layer and blocks silver deposition, limiting the number of particle shapes that can be formed.
(c) The enhanced stability of the Ag-upd layer in the presence of chloride causes growing Au-NPs to become kinetically "trapped" or "locked" into a particular facet structure early in their growth, enabling the formation of a wide variety of shapes as well as concave particles.

6.7.3 Galvanic Replacement and Underpotential Deposition

The main obstacle for the implementation of upd to a large quantity of systems is the fact that this phenomenon is usually limited to the deposition of a less noble metal on a more noble one, as it is for example the case of the Au(hkl)/Cu and Pt (hkl)/Cu systems. In the case of electrocatalytic applications, the situation is right

the opposite to the desired one, for example Cu(hkl)/Pt structures are wished. One way to circumvent this problem is to use a technique denominated galvanic replacement (gr). In 2001, Brankovic et al, followed by other groups, reported a facile route to the synthesis of Pt monolayers on Pd as base metal via gr of an upd Cu monolayer on a Pd core with a Pt precursor [46, 90, 91]. A year later, the first example of gr involving nanoscale objects was reported by Sun et al. [92]. The gr reaction is driven by the difference in electrochemical potentials, between a sacrificial template made of one metal and the ions of another metal in a solution phase [93, 94].

In the case of pure metals, galvanic corrosion is a redox process, in which a metal N is corroded by the ions of a second metal $M^{z+}_{(aq)}$ when they are in contact, in a solution phase [95]. The corrosion process can be represented by:

$$\begin{aligned} N_{(S)} &\rightarrow N^{+}_{(aq)} + e^{-} \qquad \left(E^0_1\right) \\ M^{z+}_{(aq)} + ze^{-} &\rightarrow M_{(S)} \qquad \left(E^0_2\right) \end{aligned}$$

giving the global reaction:

$$M^{z+}_{(aq)} + zN_{(S)} \rightarrow M_{(S)} + zN^{+}_{(aq)} \qquad \left(\Delta E = E^0_1 + E^0_2\right)$$

where the N metal is dissolved in solution, simultaneously with M deposition. According to Eq. (6.8), if ΔE is positive, then the corrosion reaction is driven thermodynamically.

In the case of the denominated galvanic replacement applied to upd systems, it involves oxidation and dissolution of an upd template accompanied by reduction of the ions of a second metal and deposition of the resultant atoms on the template:

$$\begin{aligned} N/S(hkl) &\rightarrow N^{+}_{(aq)} + e^{-} + S(hkl) \qquad \left(E^0_3\right) \\ M^{z+}_{(aq)} + ze^{-} + S(hkl) &\rightarrow M/S(hkl) \qquad \left(E^0_4\right) \end{aligned}$$

giving the global reaction:

$$M^{z+}_{(aq)} + N/S(hkl) \rightarrow zN^{+}_{(aq)} + M/S(hkl) \qquad \left(\Delta E = E^0_3 + E^0_4\right)$$

here, a monolayer of N initially deposited (via upd) on a S surface is dissolved simultaneously with M deposition. By manipulating stoichiometry of the participant species, it is possible to control the degree of coverage of the metal being deposited. For example, a upd monolayer of Cu deposited on a Au(111) surface may generate [90]:

- In the presence $[PtCl_4]^{2-}$, a Pt monolayer on Au(111).
- In the presence $[PtCl_6]^{2-}$, half a Pt monolayer on Au(111).

- In the presence of Ag^+, up to a bilayer of Ag on Au(111).

Galvanic corrosion and upd clearly present similarities but also important differences. Among the later, the most relevant is related to the ΔE value. The reduction couples E_1^0–E_3^0 and E_2^0–E_4^0 are different, due to the presence of the S surface.

When a metallic substrate occurs at the nanometric scale, gr can be used as a versatile and powerful method for the generation of core@shell type NPs. Park et al. in 2002 [46] (see Fig. 6.7) showed the possibility of the formation of Au@Pd and Au@Pt core@shell type NPs via gr, starting from Au@Cu NPs. Besides its employment for the formation of core@shell type NPs [46, 96–102], gr is widely used today to obtain reversed NPs, hollow particles, hollow nanorods, nanorattles, nanoboxes, alloys and dealloys, among others nanomaterial shapes [103–109]. We will return to this later.

Yu et al. [110] have reported that the electrons which are generated in the gr reaction, may accumulate mainly over specific regions of the NP. The electronic distribution that depends on geometry can be used to direct facet growth. These authors used two metallic precursors: Ag and Pd with a colloidal solution of polyhedral Au NPs. Ag reduced fast on Au-NPs to make an upd layer. Then, this core@shell was subjected to a gr process with Pd^{2+} ions. The electrons in the galvanic replacement reaction accumulate mainly at high curvature regions of the NP such as corners and borders. This preferential accumulation of electrons, which is spatially heterogeneous, directs the deposition to those regions rich in electrons. The distribution of electrons can be altered by controlling the kinetics of electron generation. A slow electron generation rate allows the electrons to accumulate only in regions of the highest curvature, that is, corners of the polyhedral NPs. On the other hand, a fast electron generation rate can disperse the electrons over a wider area, although regions of high curvature are still preferred. In this case, the electrons

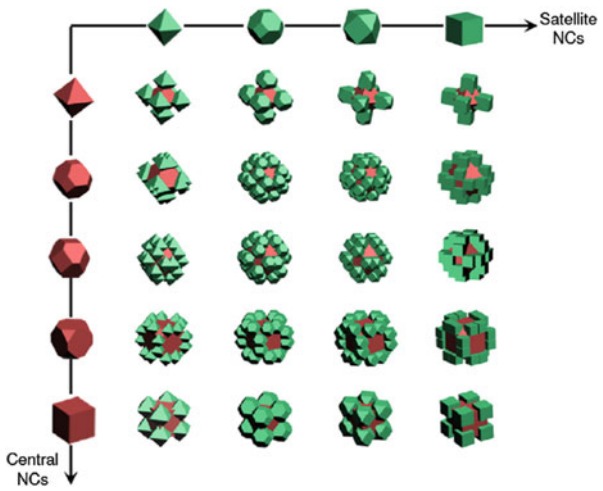

Fig. 6.24 Schematic illustration of the architectural diversity of the NP configurations that can be obtained by tuning the shapes of the central NP (*vertical axis*) and satellite NPs (*horizontal axis*) by method described in reference (Reprinted with permission from Ref. [113])

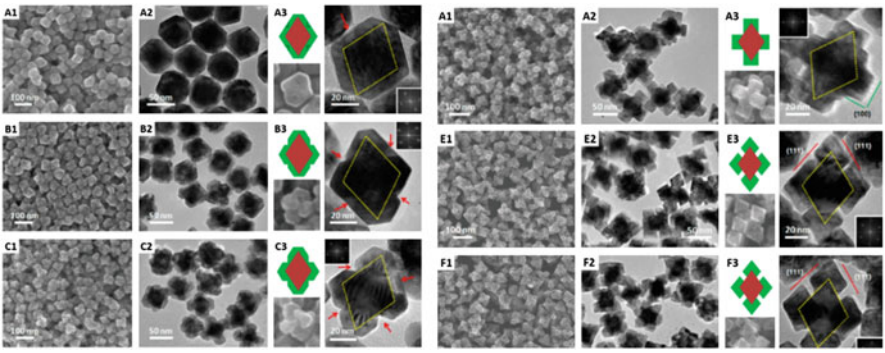

Fig. 6.25 Images obtained for the selective growth of Ag-Pd on Au NPs at different concentrations of $AgNO_3$: (**a**) 1 μM, (**b**) 3 μM, (**c**) 6 μM, (**d**) 10 μM, (**e**) 60 μM and (**f**) 80 μM. The H_2PdCl_4 concentration was 70 μM. Column 1 shows images obtained by SEM, column 2 images obtained by TEM and column 3 shows cut profiles of the geometrical models along the direction <110>. The *red arrows* show the V-shape grooves projected from the gaps and depressions (Adapted with permission from Ref. [110])

may congregate along the edges [111]. Fig. 6.24 schematically illustrates some complex nanostructures that can be obtained by using the present synthetic scheme.

The first step consists in controlling the amount of Ag adsorbed on the surface of a NP. A variable amount of Ag deposited allows a galvanic replacement variable process, as shown in SEM and TEM images for relatively low (Fig. 6.25a–c) and high (Fig. 6.25d–f) $AgNO_3$ concentrations. The Ag layer formed by "in situ" upd, is consumed by the galvanic substitution reaction and it is continuously regenerated by supplying Ag^+. This Ag- regenerative layer provides a continuous supply of electrons to the corners of the NP in order to support island growth there. A lower $AgNO_3$ concentration directs a slow formation of Ag upd, thus island growth is restricted. This is the basis of the difference between semicorner-selective deposition and full-corner-selective deposition, schematically shown in Fig. 6.26.

Figure 6.26 shows that the accumulation of electrons, and consequently the deposition along the border regions instead of corners is possible by adjusting the growth kinetics of Au and Pd in combination. Since the growth kinetics of Pd atoms favors the exposure of {100} facets and the growth kinetics of Ag atoms favors the increase in the proportion of {111} facets (see for example Fig. 6.21), each of these facet types would be preferentially exposed if the growth kinetics were dominated by that of Pd atoms or Ag atoms, respectively. With the increase of the Ag/Pd ratio, the combined growth kinetics can be modified from Pd dominance to Ag dominance. Figure 6.27 shows SEM and TEM images of core(Au)@shell(Ag-Pd) NPs at different relations of Ag^+/Pd^{2+}. At relatively low relations Ag^+/Pd^{2+}, the NP shape is truncated octahedral, showing that in synthesis conditions the exposition of facets {100} type has been favored. Under these conditions, Pd directs the growth. As the Ag^+ concentration increases, an increase in the size of facets {111} type is gradually observed indicating that Ag upd plays the key role.

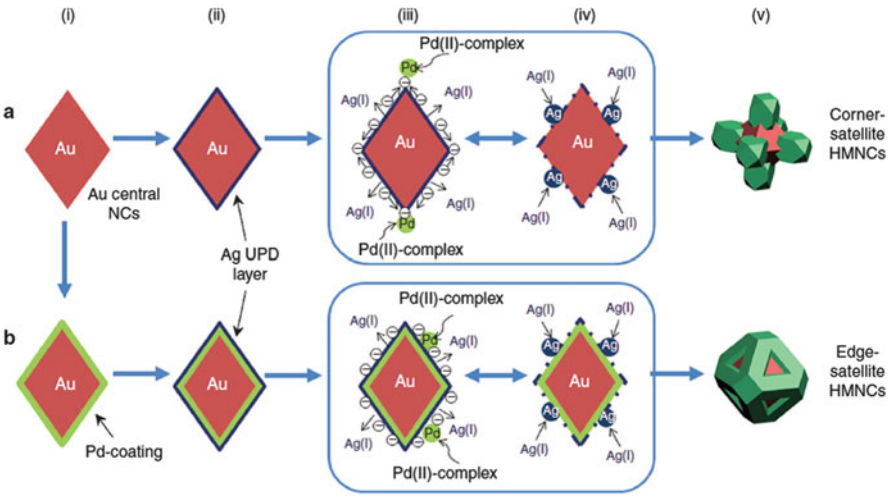

Fig. 6.26 Schematic illustrations of corner- and edge-selective depositions. The corner- and edge-selective depositions are shown in rows a and b, respectively. (*i*) Au central nanocore (NC) with a well-defined morphology. (*ii*) The Ag precursor is reduced first due to upd and a Ag monolayer is quickly formed on the central NCs. (*iii*) This in situ formed Ag layer then undergoes galvanic replacement reaction with the Pd precursor due to the difference in their reduction potentials. The electrons released by the galvanic oxidation of the Ag layer then travel and accumulate at the corners (**a**) or the edges (**b**) of the Au central NCs because of the high curvatures there. The Pd precursor is reduced and deposited preferentially on those electron-rich regions. (*iv*) The Ag layer is self-sustaining due to the swiftness of upd, that is, once the Ag atoms in the Ag layer are oxidized and dissolved, upd of Ag immediately occurs to replenish the Ag atoms lost by oxidation. The newly formed Ag upd layer is then be oxidized and regenerated. The cycle goes on (the boxed regions in *iii* and *iv*). (*v*) This cyclic process ensures a continuous supply of electrons to the corners of the central NC to sustain the reduction there. For the preparation of edge-satellite HMNCs, the surface of the Au central NCs was modified by Pd-coating (**b**(*i*)), and a Ag layer was formed on the Pd-coated Au NCs (**b**(*ii*)) (Reprinted with permission from Ref. [111])

6.7.4 Hollow Nanoparticles Through Galvanic Replacement

NPs are usually defined as polyhedra formed by facets of {111} and {100} type such as cubes, tetrahedra, octahedra, prisms, cubeoctahedra, etc. [112]. Hollow NPs (H-NPs) are nanometric scale crystals formed by facets with Miller indices {hkl} larger than the unit [88, 89, 113–116]. H-NPs surfaces are characterized by a great density of steps with low coordinated atoms, which confer large surface energy. Nanocrystals with hollow interiors and porous walls are of great interest and importance for catalytic and electrocatalytic applications, as they can provide high specific surface areas and enhanced activities relative to their solid counterparts. Galvanic replacement offers a facile and versatile approach to the generation of metal nanocrystals with hollow interiors and porous walls.

Figure 6.28 shows the main stages involved in a galvanic replacement reaction for the formation of H-NPs. When a small amount of $HAuCl_4$ is added to an

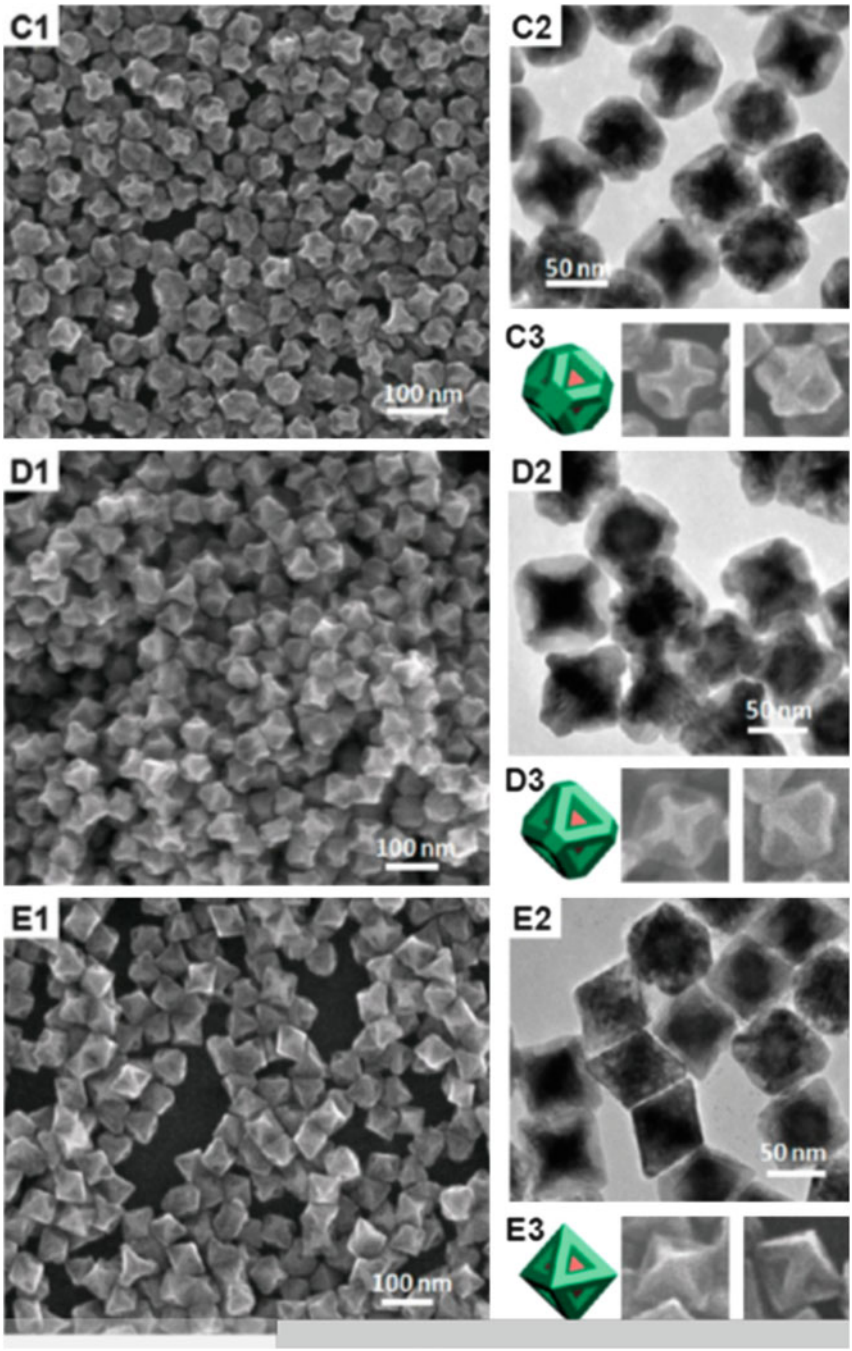

Fig. 6.27 images obtained for the selective growth at the borders shown in Fig. 6.24 and 6.26. The concentrations of $AgNO_3$ are (**c**) 20 μm, (**d**) 40 μm and (**e**) 60 μm H_2PdCl_4 concentration was 100 μm. Snapshot 1 shows images obtained by SEM, snapshot 2 images obtained by TEM and snapshot 3 shows cut profiles of the geometric models along the direction <110> and <110> (Adapted with permission from Ref. [110])

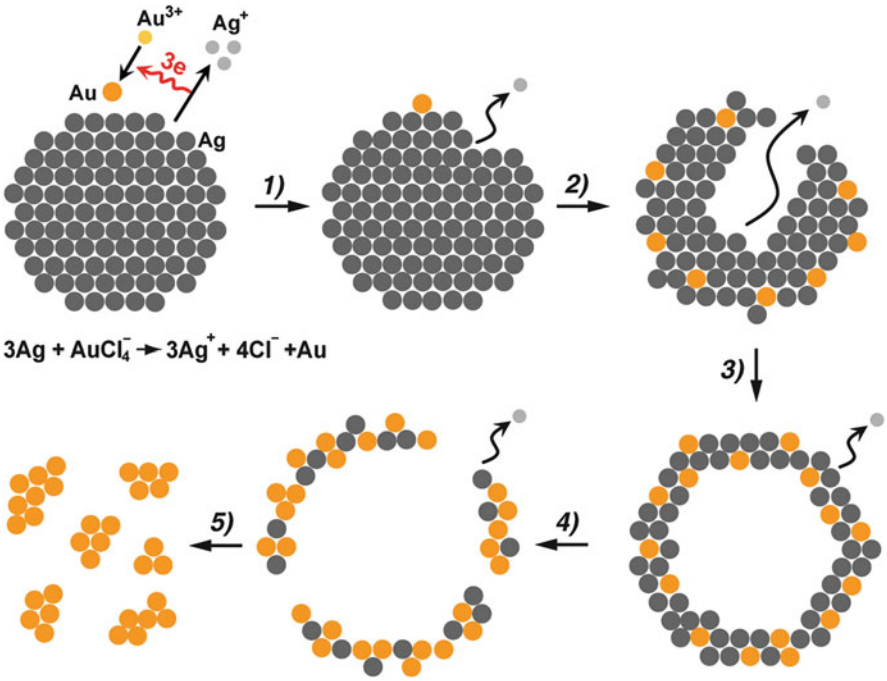

Fig. 6.28 Schematic illustration of the morphological and structural changes at different stages of the galvanic replacement reaction between a Ag nanoparticle and $HAuCl_4$ in an aqueous solution (Reprinted with permission from Ref. [124])

aqueous solution containing Ag NPs, the galvanic replacement of Ag by Au will start in the regions with large surface energy (for example, imperfections, vertex, corner regions). As a result, Ag atoms oxidize and dissolve into the solution; this generates a small hollow in the NP facet. At the same time, electrons migrate rapidly to the NP surface and are taken by $AuCl_4^-$ to generate Au atoms through a reduction reaction. Due to their similar crystal structures and lattice constants (4.086 Å vs. 4.078 Å for Ag and Au, respectively), the recently formed Au atoms tend to deposit epitaxially on the surface of the NP (step 1 in Fig. 6.28). The deposition will lead to the formation of a thin and complete Au layer on the facets of each NP that prevents the reaction of other Ag atoms with $AuCl_4^-$ below this layer, thus physically blocking the reaction. However, the small hollow generated at the beginning serves as preferential region for the continuous dissolution of Ag atoms. This hollow must have certain size that allows the income of other species allowing the galvanic replacement to take place inside the NP.

The exchange processes and /or surface diffusion may lead to a mixing of the atoms (step 2 in Fig. 6.28), since a homogeneous alloy is thermodynamically more stable than a mixture of segregated Au and Ag phases. In an intermediate state of the galvanic replacement reaction, a hollow interior and an alloy shell (step 3 in Fig. 6.28) characterizes this nanostructure. The thickness of the shell depends on

the size of the initial Ag-NP as seed (sacrificial template) as well as on the stoichiometry of the reacting Au complex. The addition of large amounts of $HAuCl_4$ to the reaction system, drives a dealloying process by selective elimination of Ag atoms from the alloy shell. This process generates many uncoordinated atoms, vacant regions, etc. which lead to a large increase in the surface free energy. These vacant regions join together, generating small hollows that coalesce and form hollow NPs. The dealloying process can also cause defragmentation of the NP into small Au clusters (step 5 in Fig. 6.28). Different SEM images can be observed in Figs. 6.29b–d, showing the different stages previously described. The addition of a chelate like $Fe(NO_3)_3$ is an alternative to favor the process of dealloying of the Au-Ag NP. This chelate dissolves Ag, generating pores in the facets, thus yielding NPs with hollow structures as can be observed in Fig. 6.29. The size of the pores can be controlled by adding a larger amount of $Fe(NO_3)_3$ as shown in the SEM images in Figs. 6.29e–g.

In 2011, Gonzáles et al. [117], reported a new application of the traditional concepts of corrosion at the nanoscale. They showed that gr together with the Kirkendall effect can be used to form hollow Au-NPs of many layers. The Kirkendall effect occurs in systems where the diffusion velocities of one on the other material are markedly different, such as Ag diffusion on Au that is larger than Au diffusion on Ag. The process begins with a picture similar to that exposed in Fig. 6.28a, b. The galvanic replacement has generated a hollow Ag cube covered by an external Au layer. Since Ag diffusion on Au is faster than Au diffusion on Ag, this produces a net flow of vacancies from the surface to the core. The concentration of vacancies increases until they coalesce in bubbles that grow at the metallic interface and join, forming a continuous cavity parallel to the cube wall. This allows the interior walls to be coated with Au. These "empty boxes" increase significantly the area/volume ratio of the material and could be used to transport or protect molecules, thus providing important applications in the fields of medicine and energy storage [118] (see Fig. 6.30a).

Trimetallic Ag-Au-Pd structures may also be produced by using the gr method together with the Kirkendall effect. The final product is a double wall nanobox with a Ag nucleus situated between the walls (see Fig. 6.30b), coated with a PdAu alloy or a Au-Pd layer, depending on the addition of the precursors being simultaneous or sequential. In the nanoboxes shown in Fig. 6.30b, Au and Ag form an alloy with interior parts richer in Ag while Pd is preferentially found at the wall surfaces.

6.7.5 Nanoparticles Growth Inside Dendrimers

In the early 2000s, Crooks and coworkers developed a technique for the generation of metallic NPs, denominated "dendrimer-encapsulated nanoparticles (DENs)" [119–121]. A scheme of this procedure is shown in Fig. 6.31.

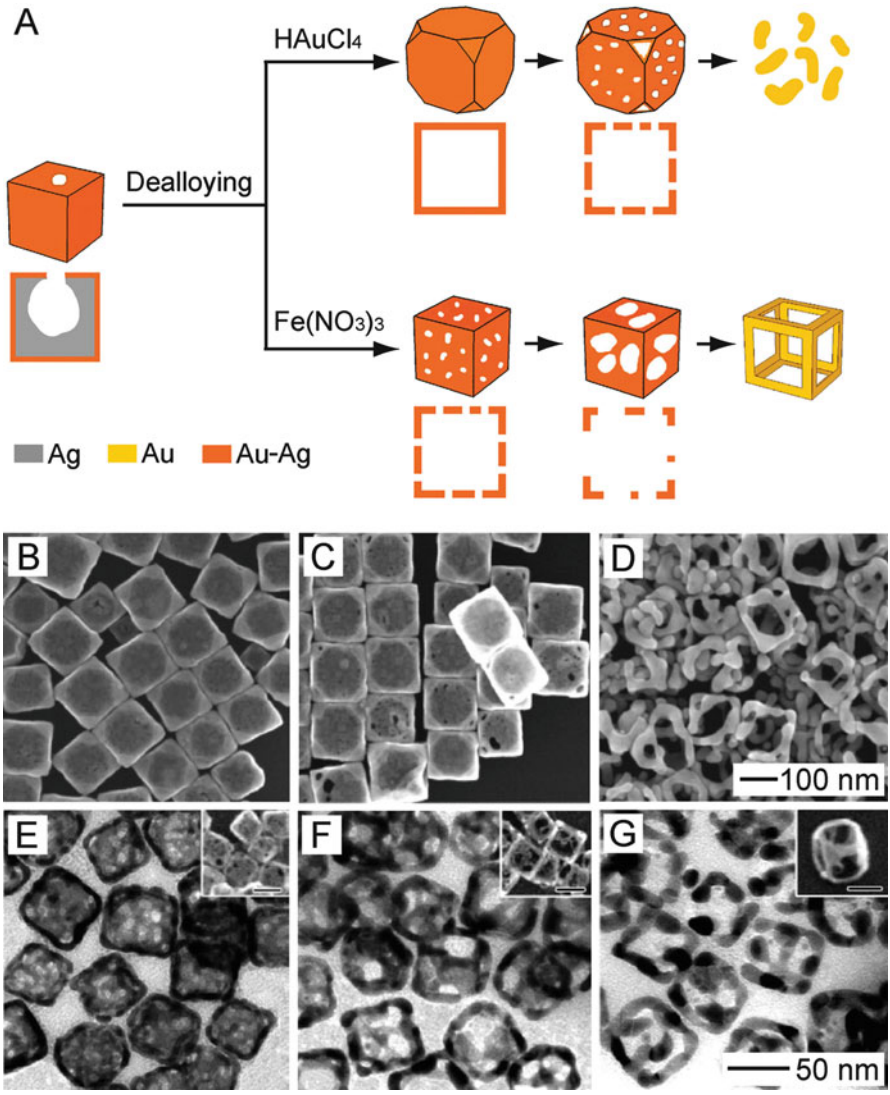

Fig. 6.29 (**a**) Schematic illustration of two different methods for dealloying involving the use of $HAuCl_4$ and $Fe(NO_3)_3$, respectively, as the etchant. (**b–d**) SEM images of samples obtained by de-alloying 120 nm partially hollow Au-Ag nanoboxes with increasing amounts of $HAuCl_4$. The 100 nm scale bar in (**d**) applies to (**b**) and (**c**). (**b–d**) are reproduced with permission from Ref. [142]. (**e–g**) TEM and SEM (insets) images of samples obtained by de-alloying 50-nm partially hollow Au-Ag nanoboxes with increasing amounts of $Fe(NO_3)_3$. The 50 nm scale bar in (**g**) applies to (**e**) and (**f**). The scale bars in the insets of (**e–g**) are 50 nm. (**e–g**) are reproduced with permission [107] (Reprinted with permission from Ref. [124])

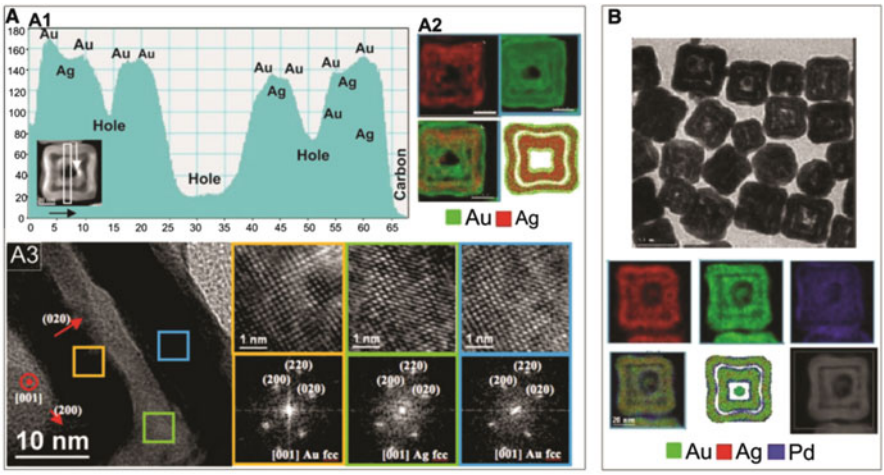

Fig. 6.30 Characterization of double wall nanoboxes. (**A1**) Intensity profile obtained on the z-contrast image of AuAg double-walled nanoboxes. (**A2**) EDX elemental map, together with a scheme of the elemental distribution. (**A3**) HRTEM characterization. (**b**) TEM image and EDX elemental maps for trimetallic PdAuAg nanoboxes (Reprinted with permission from Ref. [117])

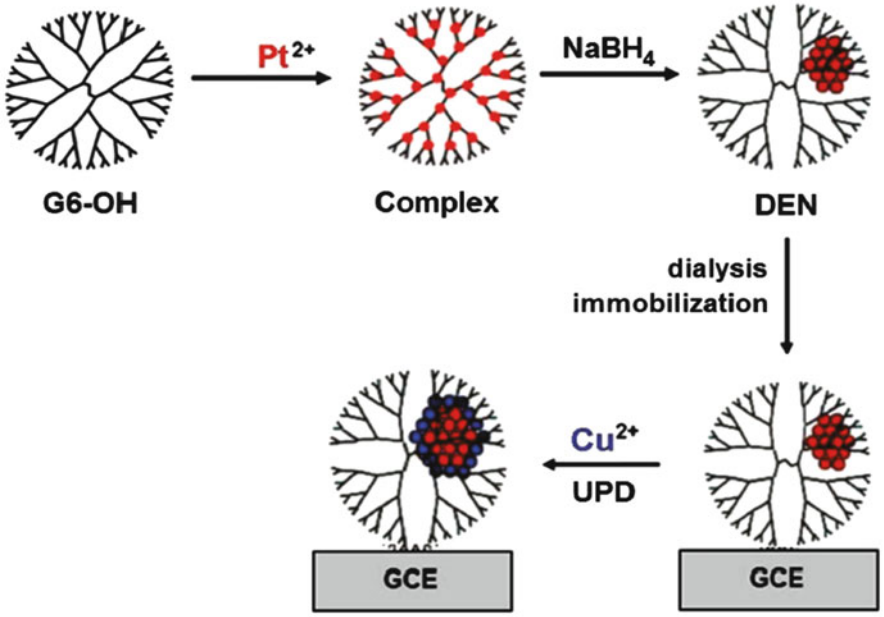

Fig. 6.31 Scheme of the dendrimer-encapsulated nanoparticles method (Reprinted with permission from Ref. [132])

In a first step, S^{2+} cations are embedded into the dendrimer matrix, yielding a complex $\left[G6-OH\left(S^{2+}\right)_n\right]$, where $G6-OH$ is a sixth-generation, hydroxyl-terminated polyamidoamine (PAMAM) dendrimer, and n is the amount of ions encapsulated in the dendrimer. The driving force for encapsulation of metal ions within dendrimers is usually based on covalent bond formation, electrostatic interactions, complexation reactions, or a combination thereof [119]. In a second step, the cations are completely reduced by using borohydride. In this way, metallic NPs were obtained within the cavities of the dendrimers. The DENs synthesis offers some significant advantages over other methods for preparing nanoparticles in very a small size range [122]. Since the cations are embedded in the polymeric matrix, the later determines the NP size. The cation/dentrimer ratio allows the adjustment of the amount of cations in the matrix and consequently, the adjustment of the final NP size. Typically, this strategy yields a NP size distribution having standard deviations of 0.3 nm [123]. This process leads to stable, nearly size-monodisperse NPs composed of Pt, Pd, Au and Cu [125–129]. It is also possible to prepare alloyed and core@shell bimetallic DENs using a slight variation of the basic approach [130, 131]. For example, PtPd bimetallic NPs containing an average of 180 atoms and being composed of seven different Pt/Pd ratios have been prepared within sixth-generation, hydroxyl-terminated, polyamidoamine dendrimers [130]. Figure 6.32a shows how the electrochemical response can be manipulated by changing the composition of a PtPd NP. For example, the current peak for oxygen reduction on the electrode modified with G6-OH(Pt_{180}) is found at 0.67 V, but the electrodes coated with bimetallic PtPd DENs having low percentages of Pd exhibit oxygen reduction reaction peaks at more positive potentials (e.g., 0.70 and 0.68 V for G6-OH($Pt_{150}Pd_{30}$) and G6-OH($Pt_{120}Pd_{60}$), respectively). Figure 6.32b summarizes the voltammetric data by showing the potential of the current peak for the oxygen reduction reaction as a function of increasing Pt percentage in each electrocatalytic particle. A maximum is reached when the NP is composed of G6-OH($Pt_{150}Pd_{30}$).

In a further step, a monolayer of a less noble metal may be electrodeposited onto the DENs by upd to yield $[G6-OH(S_n@M_m)]$. Subsequent galvanic replacement of the upd monolayer may yield different core@shell NPs. For example, Carino et al. [132] have analyzed the voltammetric behavior of Cu deposition on Pt-DENs of 55, 147, and 255 atoms, see Fig. 6.33. Their results indicate that a single atomic monolayer of Cu is deposited onto Pt DENs cores containing an average number of 147 and 225 atoms, while more than one monolayer deposits onto Pt DEN cores containing an average of 55 atoms. Two remarkable features emerge from the voltammetry of these systems:

(a) As NP size decreases, the peak potentials of anodic and cathodic processes show a shift towards lower potentials, that is, Cu upd weakens for relatively small NPs.
(b) Deposition and stripping peaks become splitted into two components.

The first behavior can be analyzed in terms of NP size. The smaller the NPs, the more important become surface effects, and the deposition potential moves to lower

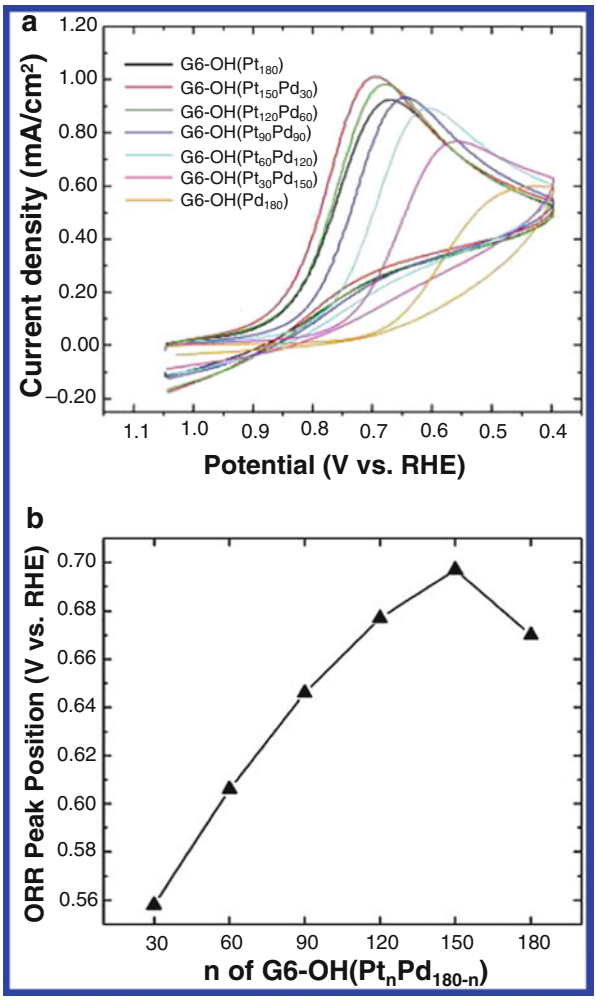

Fig. 6.32 (**a**) Cyclic voltammograms of G6-OH (Pt_nPd_{180-n}) with n = 180, 150, 120, 90, 60, 30, and 0. (**b**) A plot of the current peak position for the oxygen reduction reaction as function of n for G6-OH (Pt_nPd_{180-n}). Scan rate: 50 mV/s; electrolyte solution: aqueous 0.5 M H_2SO_4 saturated with O_2 (Reprinted with permission from Ref. [130])

potentials. This is an evidence for the extinction of the upd phenomenon at the nanoscale, analyzed in Sect. 6.7. The second behavior, the occurrence of two shoulders in the voltammograms, was assigned to the presence of different facets and/or the different behavior of borders and facets. It is known that for a very small NP it is not possible to differentiate the superficial regions into facets and borders. However, when the NP is of a bigger size, these regions may be differentiated and this fact becomes evident through this wave splitting. Very recent results by Plowman and Compton [133] confirm the extinction of Cu upd for Au NPs of 1.8 nm in citrate media.

As mentioned at the beginning of the present section, the development of NP synthesis by means of dendrimers presents two appealing aspects. On the one side, it allows the generation of metallic NPs with a very sharp size distribution. On the

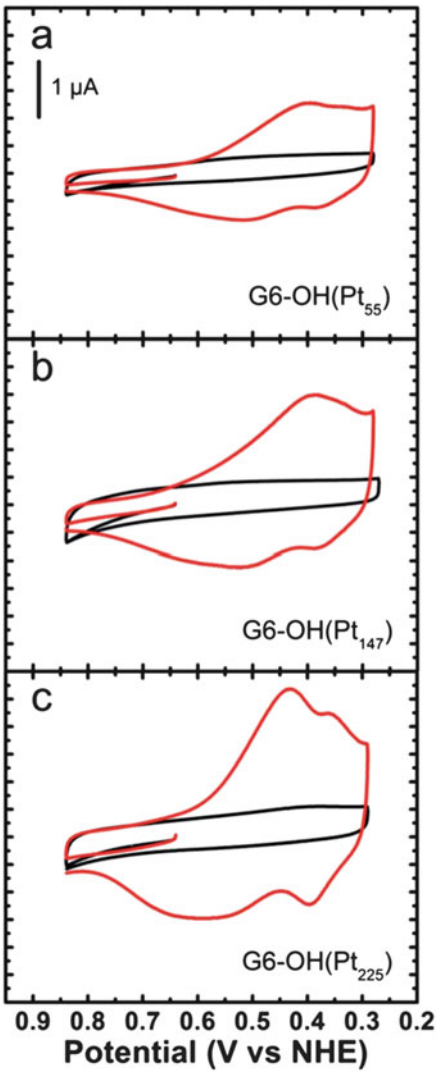

Fig. 6.33 Cyclic voltammograms obtained using G6-OH(Pt_n) DENs in aqueous electrolyte solutions containing 0.10 M H_2SO_4 + 0.010 M $CuSO_4$. The scans started at 0.64 V and were initially swept in the positive direction at a rate of 10 mV/s (Reprinted with permission from Ref. [132])

other side, this method allows the generation of metal NPs with very small sizes, between 1 nm and 2 nm. These two factors allow correlating straightforwardly experimental results with theoretical predictions. In this respect, it is worth mentioning the work of Yancey et al. [134] and Carino et al. [132]; they contrasted experimental results of electrochemical deposition with density functional (DFT) calculations for NP of similar sizes. Carino et al. [132] showed that upd of Cu onto Pt-NP(147) occurs in two steps: first onto the {100} facets (partial deposition) and then onto the {111} facets (full deposition). The partial and full shell structures were characterized by voltammetry and the experimental results were compared

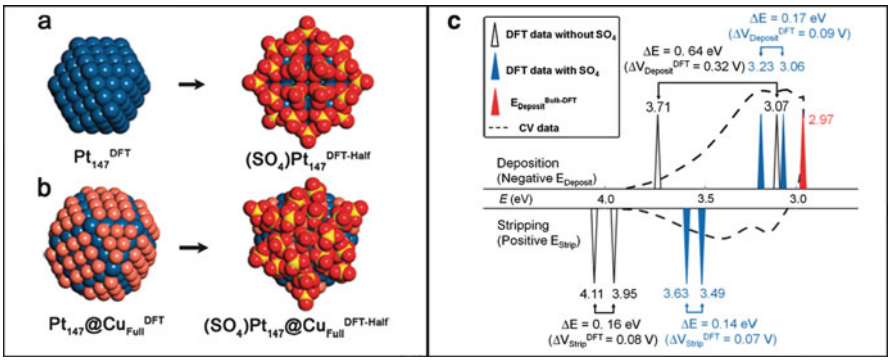

Fig. 6.34 Different models used to consider the adsorption of sulfate ions on (**a**) a Pt NP made of 147 atoms. (**b**) A core@shell NP Pt(147)@Cu(full). *Left* and *right* images show the NP without and with adsorbed SO_4 molecules respectively (**c**) DFT-calculated Cu deposition and stripping energies, as compared with the experimental voltammogram obtained for Cu upd on Pt NPs (*black dashed line*) (Reprinted with permission from Ref. [143])

with computational models generated by using DFT and molecular dynamics (MD) simulations. Figure 6.34a shows the different models used by Carino et al. [143] to emulate the Cu upd phenomena. Binding energies were calculated using DFT for Cu adsorbed on Pt{100} and Pt{111} facets of a "solvated" NP, in which SO_4 ligands were adsorbed on the surface to mimic the solvent – surface interactions existing in the experiments. The calculated binding energies were found to correspond well with the peaks observed in the CVs of Cu upd onto Pt NPs(147) (see Fig. 6.34b). In contrast, the same calculations performed on a naked, SO_4-free (solvent free) NP model did not fit the electrochemical data.

References

1. http://www.nanotechproject.org/cpi/products/. Consulted Sept 2014
2. Marie-Christine D, Didier A (2004) Chem Rev 104:293
3. Ferrando R, Jellinek J, Johnston RL (2008) Chem Rev 108(3):845
4. Drexler KE"(1986) Engines of creation: the coming era of nanotechnology, Anchor Books Editions, New York
5. Drexler KE (1992) Nanosystems: molecular machinery, manufacturing, and computatin. Wiley, New York
6. Ratner M, Ratner D (2003) Nanotechnology, a gentle introduction to the next big idea. Prentice Hall, Upper Sadle River
7. Corain B, Schmid G, Toshima N"(2008) Metal nanocluster in catalysis and materials science. Elsevier, The Netherlands
8. Castro T, Reifenberger R, Choi E, Andres RP (1990) Phys Rev B 13:8548
9. Kittel C (2005) Introduction to solid state physics, 8th edn. Wiley, Hoboken
10. Wong K, Vongehr S, Kresin VV (2003) Phys Rev B 67:035406
11. Plieth WJ (1985) Surf Sci 156:530

12. Wood DM (1981) Phys Rev Lett 46:749
13. Plieth WJ (1982) J Phys Chem 86:3166
14. Schnippering M, Carrara M, Foelske A, Kötzc R, Fermín DJ (2007) Phys Chem Chem Phys 9:725
15. Selvakannan PR, Swami A, Srisathiyanarayanan D, Shirude PS, Pasricha R, Mandale AB, Sastry M (2004) Langmuir 20:7825
16. Jana NR, Gearheart L, Murphy CJ (2001) J Phys Chem B 105:4065
17. Sánchez-Iglesias A, Carbó-Argibay E, Glaria A, Rodríguez-Gonzalez B, Pérez-Juste J, Pastoriza-Santos I, Liz-Marzán LM (2010) Chem Eur J 16:5558
18. Gentry ST, Fredericks SJ, Krchnavek R (2009) Langmuir 25:2613
19. Jiang XC, Pileni MP (2007) Colloids Surf A Physicochem Eng Asp 295:228
20. Fievet F, Lagier JP, Figlarz M (1989) MRS Bull 14:29
21. Fayet P, Granzer F, Hegenbart G, Moisar E, Pischel B, Wöste L (1985) Phys Rev Lett 55:3002
22. Foiles SM, Baskes MI, Daw MS (1986) Phys Rev B 33:7983
23. Li JH, Dai XD, Liang SH, Tai KP, Kong Y, Liu BX (2008) Phys Rep 455:1
24. Xiao L, Tollberg B, Hu X, Wang L (2006) J Chem Phys 124:114309
25. Oviedo OA, Mariscal MM, Leiva EPM (2010) Phys Chem Chem Phys 12:4580
26. Oviedo OA, Mariscal MM, Leiva EPM (2010) Electrochim Acta 55:8244
27. Perez MA (2007) In: Mariscal MM, Dassie SA (eds) Recent advances in nanoscience. Research Signpost, Trivandrum
28. LaMer VK, Dinegar RH (1950) J Am Chem Soc 17:4847
29. Iijima S, Ichihashi T (1986) Phys Rev Lett 56:616
30. Wiley B, Herricks T, Sun Y, Xia Y (2004) Nano Lett 4:1733
31. Lifshitz IM, Slyozov VV (1961) J Phys Chem Solids 19:35
32. Wagner C (1961) Zeitschrift fur Elektrochemie, Berichte der Bunsengesellschaft für physikalische Chemie 65:585. (German)
33. Erdemir D, Lee AY, Myerson AS (2009) Acc Chem Res 42:621
34. Davey RJ, Allen K, Blagden N, Cross WI, Lieberman HF, Quayle MJ, Righini S, Seton L, Tiddy GJT (2002) CrystEngComm 4:257
35. Hill TL, Chamberlin RV (1998) Proc Natl Acad Sci 95:12779
36. Hill TL (1964) Thermodynamics of small systems, part I and II. Dover Publications, New York
37. Park S, Yang P, Corredor P, Weaver MJ (2002) J Am Chem Soc 124:2428
38. Skriver HL, Rosengaard NM (1992) Phys Rev B 46:7157
39. Frisch HL (1957) J Chem Phys 27:90
40. Henglein A, Giersig M (1994) J Phys Chem 98:6931
41. Mulvaney P, Giersig M, Henglein A (1993) J Phys Chem 97:7061
42. Zsigmondy R, Anorg Z (1917) Allg Chem 99:105
43. Schmid G, West H, Malm J-O, Bovin J-O, Grenthe C (1996) Chem Eur J 2:1099
44. Budevski E, Staikov G, Lorenz WJ (1996) Electrochemical phase formation and growth – an introduction in the initial stages of metal deposition. VCH, Weinheim
45. Bochicchio D, Ferrando R (2013) Phys Rev B 87:165435
46. Park S, Weaver MJ (2002) J Phys Chem B 106(34):8667
47. Zhang B, Li J-F, Zhong Q-L, Ren B, Tian Z-Q, Zou S-Z (2005) Langmuir 21:7449
48. Lu L, Wang H, Xi S, Zhang H (2002) J Mater Chem 12:156
49. Selvakannan PR, Mandal S, Phadtare S, Gole A, Pasricha R, Adyanthaya SD, Sastry MJ (2004) J Colloid Interface Sci 269:97
50. Mandal S, Selvakannan PR, Phadtare S, Pasricha R, Sastry M (2002) Proc Indian Acad Sci Chem Sci 114:513
51. Fonticelli MH, Corthey G, Benitez GA, Salvarezza RC, Giovanetti LJ, Requejo FG, Shon YS (2007) J Phys Chem C 111:9359
52. Oviedo OA, Reinaudi L, Leiva EPM (2012) Electrochem Comm 21:14

53. Luque NB, Reinaudi L, Serra P, Leiva EPM (2009) Electrochim Acta 54:3011
54. Sharma V, Park K, Srinivasarao M (2009) Mater Sci Eng R 65:1
55. Zhang H, Jinb M, Xia Y (2012) Chem Soc Rev 41:8035
56. Goia DV, Matijevic E (1998) New J Chem 22:1203
57. Jiang XC, Brioude A, Pileni MP (2006) Colloids Surf A Physicochem Eng Asp 58277:201
58. Zsigmondy R (1917) The chemistry of colloids. Wiley, New York
59. Svedberg T (1921) The formation of colloids. D. Van Nostrand Company, New York
60. Sun Y (2013) Chem Soc Rev 42:2388
61. Carbó-Argibay E, Rodríguez-González B, Pacifico J, Pastoriza-Santos I, Pérez-Juste J, Liz-Marzán LM (2007) Angew Chem Int Ed 46:8983
62. Zhang L, Wang L, Jiang Z, Xie Z (2012) Nanoscale Res Lett 7:312
63. Sánchez-Iglesias A, Pastoriza-Santos I, Pérez-Juste I, García de Abajo FJ, Liz-Marzán LM (2006) Adv Mater 18:2529
64. Elechiguerra JL, Reyes-Gasga J, Yacaman MJ (2006) J Mater Chem 16:3906
65. Gai PL, Hammer MA (2002) Nano Lett 2:771
66. Johnson CJ, Dujardin E, Davis SA, Murphy CJ, Mann S (2002) J Mater Chem 12:1765
67. Germain V, Li J, Ingert D, Wang ZL, Pileni MP (2003) J Phys Chem B 107:8717
68. Lu LH, Wang HS, Zhou YH, Xi SQ, Zhang HJ, Hu JW, Zhao B (2002) Chem Commun
69. Lu LH, Sun GY, Zhang HJ, Wang HS, Xi SH, Hu JQ, Tian ZQ, Chen RJ (2004) J Mater Chem 14:1005
70. Zhang H, Mingshang J, Wang J, Li W, Camargo PHC, Kim MJ, Yang D, Xie Z, Xia Y (2011) J Am Chem Soc 133:6078
71. Berhault G, Bausach M, Bisson L, Becerra L, Thomazeau C, Uzio D (2006) J Phys Chem C 111:16
72. Xiong Y, McLellan JM, Yin Y, Xia Y (2007) Angew Chem Int Ed 46:790
73. Sun Y, Mayers B, Herricks T, Xia Y (2003) Nano Lett 3:955
74. Xiong Y, Chen J, Wiley B, Xia Y, Yin Y, Li Z-Y (2005) Nano Lett 5:1237
75. Xiong Y, Cai H, Wiley BJ, Wang J, Kim MJ, Xia Y (2007) J Am Chem Soc 129:3665
76. DeSantis CJ, Sue AC, Bower MM, Skrabala SE (2012) ACS Nano 6:2617
77. DeSantis CJ, Peverly AA, Peters DG, Skrabalak SE (2011) Nano Lett 11:2164
78. Huang J, Zhu Y, Lin M, Wang Q, Zhao L, Yang Y, Yao KX, Han Y (2013) J Am Chem Soc 135:8552
79. Long R, Zhou S, Wiley BJ, Xiong Y (2014) Chem Soc Rev 43:6288
80. Liu M, Guyot-Sionnest P (2005) J Phys Chem B 109:22192
81. Ikemiya N, Yamada K, Hara S (1996) Surf Sci 348:253
82. Ogaki K, Itaya K (1995) Electrochim Acta 40:1249
83. Oviedo OA, Leiva EPM, Rojas MI (2006) Electrochim Acta 51:3526
84. Grzelczak M, Pérez-Juste J, Mulvaney P, Liz-Marzán LM (2008) Chem Soc Rev 37:1783
85. Seo D, Park JC, Song H (2006) J Am Chem Soc 128(46):14863
86. Seo D, Yoo CI, Park JC, Park SM, Ryu S, Song H (2008) Angew Chem 47:763
87. Grzelczak M, Pérez-Juste J, Rodríguez-González B, Liz-Marzán LM (2006) J Mater Chem 16:3946
88. Personick ML, Langille MR, Zhang J, Mirkin CA (2011) Nano Lett 11:3394
89. Langille MR, Personick ML, Zhang J, Mirkin CA (2012) J Am Chem Soc 134:14542
90. Brankovic SR, Wang JX, Adzic RR (2001) Surf Sci 474:L173
91. Mrozek MF, Xie Y, Weaver MJ (2001) Anal Chem 73:5953
92. Sun Y, Mayers BT, Xia Y (2002) Nano Lett 2:481
93. Skrabalak SE, Chen J, Sun Y, Lu X, Au L, Cobley CM, Xia Y (2008) Acc Chem Res 41:1587
94. Lu X, Chen J, Skrabalak SE, Xia Y (2008) Proc Inst Mech Eng N 221:1
95. Hack HP (1988) Galvanic corrosion. ASTM International, West Conshohocken
96. Jin Y, Shen Y, Dong S (2004) J Phys Chem B 108(24):8142
97. Huang M, Jin Y, Jiang H, Sun X, Chen H, Liu B, Wang E, Dong S (2005) J Phys Chem B 109 (32):15264

98. Zhai J, Huang M, Dong S (2007) Electroanalysis 19:506
99. Wang L, Guo S, Zhai J, Hu X, Dong S (2008) Electrochim Acta 53:2776
100. Park Y-K, Yoo S-H, Park S (2008) Langmuir 24(8):4370
101. Peng Z, Yang H (2009) Nano Today 4:143
102. Hu J-W, Li J-F, Ren B, Wu D-Y, Sun S-G, Tian Z-Q (2007) J Phys Chem C 111(3):1105
103. Yin Y, Erdonmez C, Aloni S, Alivisatos A (2006) J Am Chem Soc 128:12671
104. Seo D, Song H (2009) J Am Chem Soc 131:18210
105. Sun Y, Wiley B, Li ZY, Xia Y (2004) J Am Chem Soc 126:9399
106. Chen J, Wiley B, McLellan J, Xiong Y, Li ZY, Xia Y (2005) Nano Lett 5:2058
107. Lu X, Au L, McLellan J, Li ZY, Marquez M, Xia Y (2007) Nano Lett 7:1764
108. Hong X, Wang D, Cai S, Rong H, Li Y (2012) J Am Chem Soc 134:18165
109. Wang Y, Wan D, Xie S, Xia X, Huang CZ, Xia Y (2013) ACS Nano 7:4586
110. Yu Y, Zhang Q, Yao Q, Xie J, Lee JY (2013) Chem Mater 25:4746
111. Yu Y, Zhang Q, Xie J, Lee JY (2013) Nat Commun 4:1454
112. Wales D (2004) Energy landscapes applications to clusters, biomolecules and glasses. Cambridge Molecular Science. Royal Society of Chemistry. http://pubs.rsc.org/en/journals/journalissues/fd?_ga=1.53658280.1007409239.1445285929#!recentarticles&adv
113. Tian N, Zhou Z-Y, Sun S-G, Ding Y, Wang ZL (2004) Science 316:732
114. Tian N, Zhou Z-Y, Sun S-G (2008) J Phys Chem C 112:19801
115. Zhou Z-Y, Tian N, Huang Z-Z, Chen D-J, Sun S-G (2008) Faraday Discuss 140:81
116. Hong JW, Kim M, Kim Y, Han SW (2012) Chem Eur J 18:16626
117. González E, Arbiol J, Puntes VF (2011) Science 334:1377
118. Liu J, Qiao SZ, Chen JS, Wen X, Lou D, Xing X, Lu GQM (2011) Chem Commun 47:12578
119. Crooks RM, Zhao M, Sun L, Chechik V, Yeung LK (2001) Acc Chem Res 34:181
120. Crooks RM, Chechik V, Lemon BI III, Sun L, Yeung LK, Zhao M (2002) Synthesis, characterization, and applications of dendrimer-encapsulated metal and semiconductor nanoparticles. In: Feldheim DL, Foss CA Jr (eds) Metal nanoparticles- synthesis, characterization, and applications. Marcel Dekker, New York
121. Scott RWJ, Wilson OM, Crooks RM (2005) J Phys Chem B 109:692
122. Myers VS, Weir MG, Carino EV, Yancey DF, Pande S, Crooks RM (2011) Chem Sci 2:1632
123. Ye H, Crooks RM (2007) J Am Chem Soc 129:3627
124. Xia X, Wang Y, Ruditskiy A, Xia Y (2013) Adv Mater 25:6313
125. Zhao M, Crooks RM (1999) Angew Chem Int Ed 38:364
126. Ye H, Crooks RM (2005) J Am Chem Soc 127:4930
127. Wilson OM, Knecht MR, Garcia-Martinez JC, Crooks RM (2006) J Am Chem Soc 128:4510
128. Garcia-Martinez JC, Lezutekong R, Crooks RM (2005) J Am Chem Soc 127:5097
129. Zhao M, Sun L, Crooks RM (1998) J Am Chem Soc 120:4877
130. Scott RWJ, Wilson OM, Oh S-K, Kenik EA, Crooks RM (2004) J Am Chem Soc 126:15583
131. Wilson OM, Scott RWJ, Garcia-Martinez JC, Crooks RM (2005) J Am Chem Soc 127:1015
132. Carino EV, Crooks RM (2011) Langmuir 27:4227
133. Plowman BJ, Compton RG (2014) ChemElectroChem 1:1009
134. Yancey DF, Zhang L, Crooks RM, Henkelman G (2012) Chem Sci 3:1033
135. Oviedo OA, Vélez P, Macagno VA, Leiva EPM (2014) Surf Sci 631:23
136. Mariscal MM, Oviedo OA, Leiva EPM (2012) J Mater Res 27:1777
137. Oviedo OA, Leiva EPM, Mariscal MM (2008) Phys Chem Chem Phys 10:3561
138. Campbell FW, Zhou Y, Compton RG (2010) New J Chem 34:187
139. Campbell FW, Compton RG (2010) Int J Electrochem Sci 5:407
140. Zhou Y, Rees NV, Compton RG (2012) ChemPhysChem 12:2085
141. Oviedo OA, Reinaudi L, Mariscal MM, Leiva EPM (2012) Electrochim Acta 76:424
142. Sun Y, Xia Y (2004) J Am Chem Soc 126:3892
143. Carino EV, Kim HY, Henkelman G, Crooks RM (2012) J Am Chem Soc 134:4153